

# Journal of Energy

ISSN 1849-0751 (On-line)  
ISSN 0013-7448 (Print)  
UDK 621.31

<https://doi.org/10.37798/EN2024732>

VOLUME 73 Number 2 | 2024

- 03** Toni Pohovski, Vjenceslav Kuprešanin, Filip Razum, Davor Švarc, Matej Dorešić  
Automated Measurement System of High Accuracy for Shunt Reactors
- 08** Dino Kovačević, Mladen Marković, Damir Blažina  
Numerical Calculation and Direct Measurement of Local Hot Spot Temperatures in Transformer Clamping Plates
- 13** Mouctar Tchakala, Tahar Tafticht, Iqbal Messaïf, Md Jahidur Rahman  
Regression Learner Application Model-Based Short-Term Load Forecasting for Mascouche (Quebec, Canada)
- 21** Bruno Jurišić, Marijan Perković, Ivan Novko, Luka Kovačić, Igor Žiger, Tomislav Župan  
Proposal of Testing Procedure for Resonance and Ferroresonance Inception Possibility in Instrument Transformers
- 25** Dragan Poljak, Tonko Garma, and Zorica Novakovic Šesnić  
Several Aspects of Human Exposure to Low Frequency Fields; Incident and Internal Field Dosimetry Procedures and Related Legal Issues

# Journal of Energy

Scientific Professional Journal Of Energy, Electricity, Power Systems

Online ISSN 1849-0751, Print ISSN 0013-7448, VOL 73

<https://doi.org/10.37798/EN2024732>

## Published by

HEP d.d., Ulica grada Vukovara 37, HR-10000 Zagreb

HRO CIGRE, Berislavićeva 6, HR-10000 Zagreb

## Publishing Board

Robert Krklec, (president) HEP, Croatia,

Božidar Filipović-Grčić, (vicepresident), HRO CIGRE, Croatia

## Editor-in-Chief

Igor Kuzle, University of Zagreb, Croatia

## Associate Editors

Murat Fahrioglu, Middle East Technical University, Cyprus

Tomislav Gelo University of Zagreb, Croatia

Davor Grgić University of Zagreb, Croatia

Marko Jurčević University of Zagreb, Croatia

Marija Šiško Kuliš HEP-Generation Ltd., Croatia

Goran Majstrovic Energy Institute Hrvoje Požar, Croatia

Tomislav Plavšić Croatian Transmission system Operator, Croatia

Goran Slipac HEP-Distribution System Operator, Croatia

Matija Zidar University of Zagreb, Croatia

## International Editorial Council

Anastasios Bakirtzis Aristotle University of Thessaloniki, Greece

Fino Barbir University of Split, Croatia

Lina Bertling Tjernberg, KTH Royal Institute of Technology, Sweden

Tomislav Capuder University of Zagreb, Croatia

Maja Muftić Dedović, University of Sarajevo, Bosnia and Herzegovina

Martin Dadić University of Zagreb, Croatia

Tomislav Dragičević, Technical University of Denmark, Denmark

Ante Elez Končar-Generators and Motors, Croatia

Dubravko Franković University of Rijeka, Croatia

Hrvoje Glavaš J. J. Strossmayer University of Osijek, Croatia

Mevludin Glavić University of Liege, Belgium

Božidar Filipović Grčić University of Zagreb, Croatia

Josep M. Guerrero, Technical University of Catalonia, Spain

Juraj Havelka University of Zagreb, Croatia

Dirk Van Hertem KU Leuven, Belgium

Žarko Janić Siemens-Končar-Power Transformers, Croatia

Dražen Lončar, University of Zagreb, Croatia

Jovica Milanović, University of Manchester, UK

Viktor Milardić University of Zagreb, Croatia

Damir Novosel Quanta Technology, USA

Hrvoje Pandžić University of Zagreb, Croatia

Ivan Pavić, University of Luxembourg, Luxembourg

Vivek Prakash Banasthali Vidyapith, India

Ivan Rajšl University of Zagreb, Croatia

Damir Sumina University of Zagreb, Croatia

Zdenko Šimić Paul Scherrer Institut, Switzerland

Bojan Trkulja University of Zagreb, Croatia

## EDITORIAL

The first paper is “Automated Measurement System of High Accuracy for Shunt Reactors”. The paper discusses why standard transformer measurement systems are less suitable for measuring shunt reactor losses. It includes examples of uncertainty calculations for different measurement systems and power factors. The paper compares the accuracy of shunt reactor loss measurements with two systems: a newly integrated shunt reactor measurement system and the standard transformer measurement system. The Automated Transformer Test (ATT) system contains modules for shunt reactor measurements. These measurements include loss measurement, impedance measurement, linearity test, zero-sequence impedance measurement, winding resistance measurement, temperature rise test and mutual reactance measurement. While the ATT software already covers most electrical type and routine tests for power transformers, it has now been extended to support comprehensive shunt reactor testing, improving its functionality and scope.

The second paper is “Numerical Calculation and Direct Measurement of Local Hot Spot Temperatures in Transformer Clamping Plates”. The paper presents a multiphysics approach that combines electromagnetic and thermal modeling to analyze local hot-spot temperatures in transformer clamping plates. This methodology has been validated by direct measurement using fiber optic temperature probes, proving its accuracy and reliability. The simulation results closely match experimental measurements, confirming the accuracy of the model in predicting the temperature behavior. Future studies could investigate transformers with higher short-circuit impedances, possibly identifying tap position 1 as less favorable. The developed multiphysics model uses the finite element method (FEM) to calculate the stray field losses in the clamping plates through a nonlinear impedance boundary condition and computational fluid dynamics (CFD) to simulate the hot-spot temperatures.

The third paper is “Regression Learner Application Model-Based Short-Term Load Forecasting for Mascouche (Quebec, Canada)”. This paper presents a real-time case study for the Mascouche region using a regression learner application for short-term load forecasting. The study focuses on short-term load forecasting using the regression method, which provides valuable business insights. Load forecasting is essential for optimal operation of the power grid and enables utilities to address technical and economic challenges. A forecasting model with low prediction errors reduces operating costs and risks and optimizes models. Actual load and weather data from the Hydro-Quebec database are used to explore this method’s capabilities, advantages, and limitations, with a focus on the Mascouche region in Quebec, Canada, where the load fluctuates between 60 and 140 megawatts.

The fourth paper is “Proposal of Testing Procedure for Resonance and Ferroresonance Inception Possibility in Instrument Transformers”. This paper examines the potential for ferroresonance in the interaction between circuit breakers and inductive instrument transformers. The current standards lack guidance on testing ferroresonance behavior. Therefore, the paper proposes a standardized testing procedure and presents measurements on a full-scale system. EMTP simulations complement these measurements to analyze a more comprehensive network topology, in particular the capacitance combinations of circuit breakers. These simulations, validated for a 170 kV voltage transformer and a combined instrument transformer, show an accuracy within 10%. EMTP modeling is also applied to a 420 kV voltage power transformer during the design phase to ensure that it does not experience ferroresonance. The study provides a practical approach for testing and simulating ferroresonance in inductive instrument transformers, thus increasing the safety of power networks.

The last paper is “Several aspects of Human Exposure to Low Frequency Fields; Incident and Internal Field dosimetry Procedures and Related Legal issues”. This paper presents simple and efficient dosimetry procedures for human exposure to low-frequency (LF) electric and magnetic fields at single and multiple frequencies. The primary electromagnetic interference (EMI) sources studied are overhead power lines and transmission substations. Electric and magnetic fields from these sources are either calculated or measured. Theoretical dosimetry for electric fields uses the Scalar Potential Integral Equation (SPIE), while magnetic fields are calculated using the Biot-Savart law. The article gives an overview of incident and internal field dosimetry techniques using simplified body models and discusses the associated legal issues and exposure limits according to national and international legislation.

Igor Kuzle  
Editor-in-Chief

# Automated Measurement System of High Accuracy for Shunt Reactors

Toni Pohovski, Vjenceslav Kuprešanin, Filip Razum, Davor Švarc, Matej Dorešić

**Summary** — System for automated transformer tests (ATT) enables different measurements on power transformers, from simple to the most complex, with a high degree of automation. ATT system is now expanded with modules for measurements on shunt reactors. The measurements related to shunt reactors that are covered with the system are: measurement of losses, impedance measurement, linearity test, zero impedance measurement, winding resistance measurement, temperature rise test and measurement of mutual reactance. Besides the measurement, ATT enables data analysis and report generation, all in accordance with [1,2]. Measurement of shunt reactor losses with satisfactory accuracy is a big challenge due to power factors of the reactors as low as 0,001. A system for loss measurements with high accuracy, consisting of measuring bridge, current comparator and standard capacitor is integrated into ATT. In the paper, a comparison in terms of loss measurement accuracy on shunt reactor is given for two measurement systems – a newly integrated system for shunt reactors and standard system used for transformer measurements.

**Keywords** — Shunt reactors, automated tests, high accuracy, measurement uncertainty

## I. INTRODUCTION

Shunt reactors [3,4] are components of electrical energy system used to compensate for capacitive power generated by long overhead lines or extended cable networks. Conceptually, shunt reactors are similar to transformers, but with only one (single-phase or three-phase) winding.

Significant changes need to be made in the transformer test field to meet the requirement of shunt reactor testing – changes in test equipment, measurement system and ATT software. Although the equipment beyond measuring components is not subject of this paper, a short description of test circuit is given. The measurement system used for transformer loss measurements consists of instrument transformers and power analyzer. When choosing the components of measurement system, special attention was paid to obtain loss measurements with satisfactory accuracy, even in the case of low power factor. Measurement of shunt reactor losses represents great challenge because the power factor in these cases can be as low as 0,001. Since satisfactory accuracy can't be reached

with conventional instrument transformers, a new special high accuracy system has been purchased, consisting of three sets of instruments. Each set consists of HV measuring bridge with standard capacitor and current comparator. Although the primary purpose of HV measuring bridge is measurement of capacitance and  $\tan\delta$ , here they are used as a part of loss measurement system. In the paper, an explanation is given why standard transformer measurement system is less appropriate for shunt reactor loss measurements. Examples of uncertainty calculations are given for different measurement systems and different power factors.

## II. MEASUREMENT ACCURACY AND SELECTION OF THE MEASUREMENT SYSTEM

It is in the interest of both the test engineer and the customer to achieve measurement result of the highest quality, i.e., a measurement result with the lowest measurement uncertainty possible. A higher quality measurement result reduces risk of accepting the product which exceeds the guaranteed values, which means reduced risk for the customer, but also reduces the risk of rejecting the product which satisfies guaranteed values, which is in the interest of the manufacturer. A higher quality measurement may also enable a more quality design of the product which leads to saving in material and finally to a less expensive product [5]. These statements hold even if the decision of accepting/rejecting the product rely only on best estimate of measurement result, without considering measurement uncertainty [6]. On the other hand, more accurate measurement equipment is more expensive, as well as its maintenance and calibration [7]. What is a satisfactory measurement uncertainty can be defined by the standard or the decision is made between the transformer manufacturer and the customer.

IEC/TS 60076-19:2013 [8] gives the procedure for the estimation of uncertainties in the measurement of the losses of power transformers and reactors. Mathematical model for the measurement of losses can be expressed as:

$$P_L = k_{CN} \frac{1}{1 + \frac{\varepsilon_C}{100}} \cdot k_{VN} \frac{1}{1 + \frac{\varepsilon_V}{100}} \cdot \frac{P_W}{1 - (\Delta_{\phi V} - \Delta_{\phi C}) \tan\phi} \quad (1)$$

where  $k_{CN}$  and  $k_{VN}$  denote rated ratios of current and voltage transformer respectively,  $\varepsilon_C$  and  $\varepsilon_V$  are corresponding ratio errors,  $P_W$  is the reading of power analyzer and  $\Delta_{\phi V}$  and  $\Delta_{\phi C}$  denote angle errors of instrument transformers. Since the aim of this paper is to make comparison of measured losses, without concerning contributions specific to load losses and no-load losses, a mathematical model given in equation (1) is slightly different from those given in technical specifications [6] for load losses

(Corresponding author: Toni Pohovski)

Toni Pohovski, Vjenceslav Kuprešanin and Filip Razum are with the Končar - Electrical Engineering Institute Ltd., Zagreb, Croatia (e-mails: [tpohovski@koncar-institut.hr](mailto:tpohovski@koncar-institut.hr), [vkupresa@koncar-institut.hr](mailto:vkupresa@koncar-institut.hr), [frazum@koncar-institut.hr](mailto:frazum@koncar-institut.hr))

Davor Švarc and Matej Dorešić are with the Končar - Power Transformers Ltd., A joint venture of Siemens and Končar, Zagreb, Croatia (e-mails: [davor.svarc@siemens-energy.com](mailto:davor.svarc@siemens-energy.com), [matej.doresic@siemens-energy.com](mailto:matej.doresic@siemens-energy.com))

and no-load losses.

Based on mathematical model (1) expression for measurement uncertainty of losses can be written as:

$$u_{\%P} = \sqrt{u_{\%C}^2 + u_{\%V}^2 + u_{\%PW}^2 + u_{\%FD}^2} \quad (2)$$

where  $u_{\%C}$  is the uncertainty of current transformer ratio,  $u_{\%V}$  is uncertainty of voltage transformer ratio,  $u_{\%PW}$  is uncertainty of power indicated by the analyzer and  $u_{\%FD}$  denotes measurement uncertainty that affects the phase displacement correction  $F_D$ .

In the next, a parallel comparison in terms of loss measurement uncertainty is made for two measurement systems – transformer loss measurement system and system with single-phase measuring bridge.

### A. ACCURACY OF TRANSFORMER LOSS MEASUREMENT SYSTEM

Transformer loss measurement system (TLMS) of high accuracy consists of three main components, each of them contributing to loss measurement uncertainty:

- power analyzer,
- voltage transformer
- current transformer

Uncertainty component for power analyzer  $u_{\%PW(AS)}$  is estimated based on limits of errors. Limits of error for power analyzers, provided by different manufacturers, differ a lot. General expression for power analyzers can be always expressed in the form:

$$G_{PA}(P)\% = G_{PA}(V)\% + G_{PA}(I)\% + G_{PA}(\cos\varphi)\% \quad (3)$$

where  $G_{PA}(P)\%$  is limit of error for active power,  $G_{PA}(V)\%$  is limit of error for voltage channel,  $G_{PA}(I)\%$  is limit of error for current channel and  $G_{PA}(\cos\varphi)\%$  is limit of error due to angle error. Uncertainty of power measured with power analyzer (PA),  $u_{\%PW}$ , is:

$$u_{\%PW(PA)} = \frac{G_{PA}(P)\%}{\sqrt{3}} \quad (4)$$

Uncertainty components due to ratio errors of voltage transformer ( $u_{\%V}$ ) and current transformer ( $u_{\%C}$ ) are:

$$u_{\%V} = \frac{G_{\%V}}{\sqrt{3}} \quad (5)$$

$$u_{\%C} = \frac{G_{\%C}}{\sqrt{3}} \quad (6)$$

where error of limits for voltage transformer  $G_{\%V}$  and current transformer  $G_{\%C}$  are given in technical specification of instrument transformers.

The uncertainty  $u_{FD}$  that affect the phase displacement correction  $F_D$  for practical application can be estimated by the following simplified relation [6]:

$$u_{\%FD} \approx u_{\Delta\varphi} \cdot \tan\varphi \cdot 100 \% \quad (7)$$

where  $u_{\Delta\varphi}$  represents the combined uncertainty of the instrument transformer phase displacement that may be determined by:

$$u_{\Delta\varphi} = \sqrt{\left[\frac{G_{\Delta\varphi V}}{\sqrt{3}}\right]^2 + \left[\frac{G_{\Delta\varphi C}}{\sqrt{3}}\right]^2} \quad (8)$$

where the limits of angle error for voltage transformer  $G_{\Delta\varphi V}$  and current transformer  $G_{\Delta\varphi C}$  are given in technical specification of instrument transformers.

### B. ACCURACY OF SYSTEM WITH MEASURING BRIDGE

System with single-phase measuring bridge (MBS) for loss measurement consists of:

- measuring bridge
- standard capacitor
- current comparator

Measuring bridge and standard capacitor are in manufacturer's specifications treated as one unit, with given limits of errors for voltage  $G_{MB}(V)\%$ , for current  $G_{MB}(I)\%$  and for power factor  $G_{MB}(\cos\varphi)\%$ . Based on this specification, uncertainty of power measurement with measuring bridge and standard capacitor is calculated as:

$$u_{\%PW(MB)} = \frac{1}{\sqrt{3}} \cdot \sqrt{G_{MB}(V)\%^2 + G_{MB}(I)\%^2 + G_{MB}(\cos\varphi)\%^2} \quad (9)$$

Current comparator contributes to overall uncertainty of losses measurement with amplitude  $G_{\%C}$  and angle  $G_{\Delta\varphi C}$  limits of error which should be inserted in equations (6) and (8) respectively.

### C. ANALYSIS OF MEASUREMENT UNCERTAINTY FOR LOSSES

Measurement of shunt reactor losses with satisfactory accuracy is a big challenge due to low power factors. Dominant contributors to measurement uncertainty of losses in case of Transformer loss measurement system used are angle errors  $G_{\Delta\varphi V}$  and  $G_{\Delta\varphi C}$  of instrument transformers, considered by component  $u_{FD}\%$  in equation (2), and the uncertainty of power measured with power analyzer  $u_{\%PW(AS)}$ . With neglecting the amplitude errors of instrument transformers, measurement uncertainty of losses can be expressed as:

$$U(P)\% \approx \sqrt{u_{\%PW}^2 + u_{\%FD}^2} \quad (10)$$

If power analyzer LEM-NORMA D6133TE [9] is used in TLMS limit of error can be expressed as:

$$G(P)\% = G(V)\% + G(I)\% + 0,00358 \cdot \tan\varphi \% \quad (11)$$

And for low power factor uncertainty component can be approximated as:

$$u_{\%PW(PA)} = \frac{G_{PA}(P)\%}{\sqrt{3}} \approx \frac{0,00358 \cdot \tan\varphi \%}{\sqrt{3}} \quad (12)$$

Finally, expanded measurement uncertainty of TLMS is:

$$U(P)_{TLMS\%} \approx \frac{2 \cdot 10^{-4} \cdot \tan\varphi}{\sqrt{3}} \cdot \sqrt{\left[G_{\Delta\varphi V}\right]^2 + \left[G_{\Delta\varphi C}\right]^2 + [35,8] \%} \quad (13)$$

When measuring power losses with MBS, dominant influence is measurement uncertainty of measuring bridge ( $u_{\%PW(MB)}$ ), while amplitude and angle error of current comparator can be neglected. Therefore, expanded measurement uncertainty ( $k=2$ ) for losses in case of MBS can be calculated as:

$$U(P)_{MBS\%} \approx \frac{2}{\sqrt{3}} \left( \sqrt{0,2^2 + 0,1^2 + 0,5^2 + \frac{1 \cdot 10^{-3}}{\cos \varphi} + \left( \frac{1 \cdot 10^{-3}}{\cos \varphi} \right)^2} \right) \% \quad (14)$$

Comparison of power loss uncertainties for two systems (TLMS, MBS) in dependency of power factor (PF) is given in Fig 1. It can be clearly seen that the expanded uncertainties for power factor of 0,01 are practically the same, but as power factor goes down to 0,001, MBS assures substantially more accurate measurement. Uncertainties given in Fig 1 are for each phase separately. In case of three-phase power loss measurement, with approximately the same losses measured in each phase, expanded uncertainty of total losses would be  $\sqrt{3}$  times smaller.

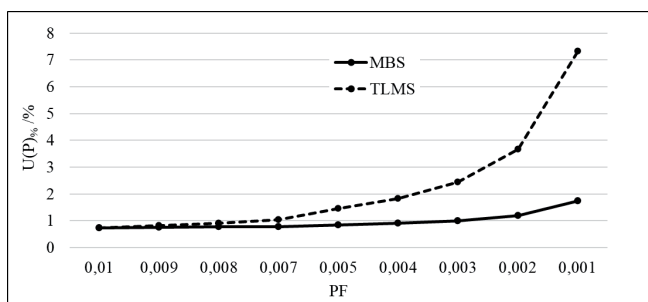


Fig. 1. Comparison of power loss measurement uncertainty (single-phase) for two measurement systems: TLMS and MBS

### III. AUTOMATED MEASUREMENT SYSTEM FOR SHUNT REACTORS

Software for Automated Transformer Test (ATT) enables different tests on power transformers, from simple to the most complex, with a high degree of automation. ATT leads test engineers through measurements, checks functionality of the measurement system, automatically measures different values (currents, voltages, losses, temperatures), perform analysis, saves data to the files, and generate test reports.

ATT enables communication with measuring equipment. Be-

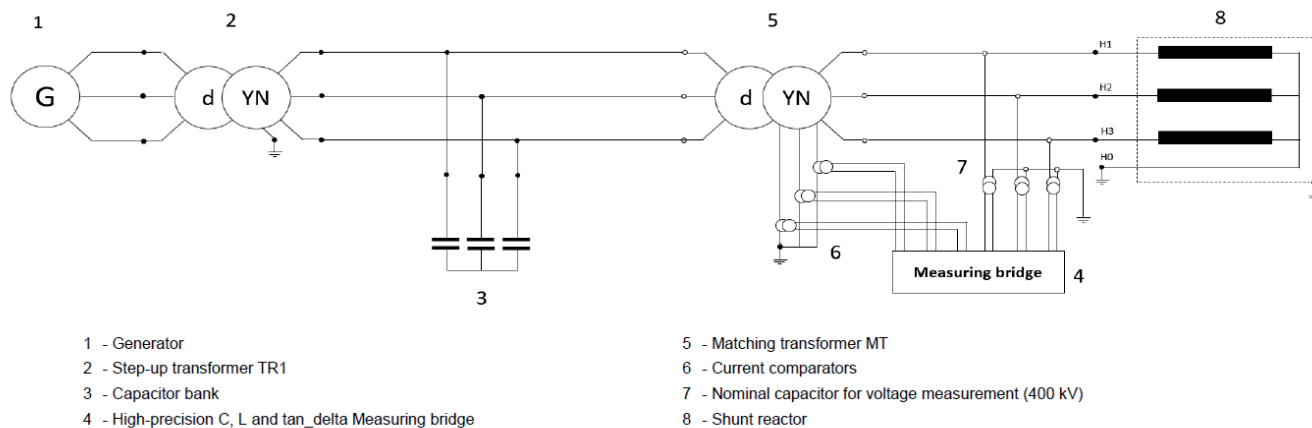


Fig. 3. Basic measurement principles

sides standard equipment for measurement of transformer losses (power analyzers, current transformers, voltage transformers), ATT supports communication with digital thermometers, voltmeters, and other types of instruments for special purposes. Expansion of ATT software with modules for shunt reactors also implied integration of system with measuring bridge, to assure shunt reactor loss measurements with satisfactory accuracy in case of very low power factor.

#### A. COMMUNICATION AND MEASUREMENT PRINCIPLES

Measurement bridge in combination with current comparator and standard capacitor enables single-phase measurement. Although it is possible cover three phase shunt reactors with single-phase measurement, such measurements would be less accurate and highly time demanding, also with modifications in measurement procedure. KPT test bay requirement on fast, simultaneous and accurate measurements for both single-phase and three-phase shunt reactors resulted in integration of three measuring bridge into one system.

Basic communication principle is given in Fig 2. Each measuring bridge communicates with corresponding software over ethernet card. Since only one special purpose software can be installed on personal computer (PC), three PCs are required for a three-phase measurement system. ATT as a client software communicates with measuring bridges indirectly, by using interface of corresponding software. Task for ATT is to configure equipment for measurement, to collect and analyse data according standards [1] and to generate test report.

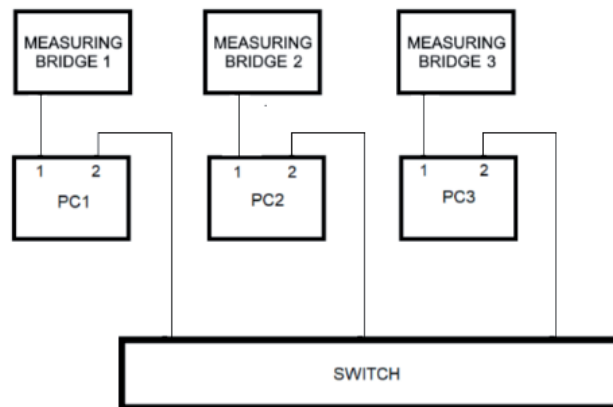


Fig. 2. Basic communication principles

The principal scheme for measurement of losses and impedance for shunt reactors is given in Fig. 3. Testing of shunt reactors puts high requirements on measuring equipment, since most of the test are performed at rated voltage, at maximum operating voltage or even at higher voltage level in case of induced voltage test. Compared to transformer tests, the AC source must be stronger. Requirements on high reactive power at high voltage levels are satisfied by use of specially designed matching transformer. As already explained, measuring bridge is used for highly accurate measurement of shunt reactor losses. Since the test currents of shunt reactors are substantially higher than the measuring bridge rated current, a current comparator is used in each phase to level down the test current. The test voltage is measured indirectly by measuring current flowing through the standard (nominal) capacitor. Capacitor bank put between the step-up transformer and matching transformer is used to compensate high amount of reactive power.

### B. ATT FOR SHUNT REACTORS

Main window of ATT software for shunt reactors is given in Fig 4. It contains of 6 main parts:

- *Hardware test* – testing communication with instruments included in software
- *Reactors* –selection, power reactors or transformers
- *Reactor Data* – input data of power reactor on test
- *Measurement* – 9 different modules
- *Analysis* – 2 different modules
- *Print* – test report generation for all tests (test report for customer or draft report for research and development)



Fig. 4. ATT – main window

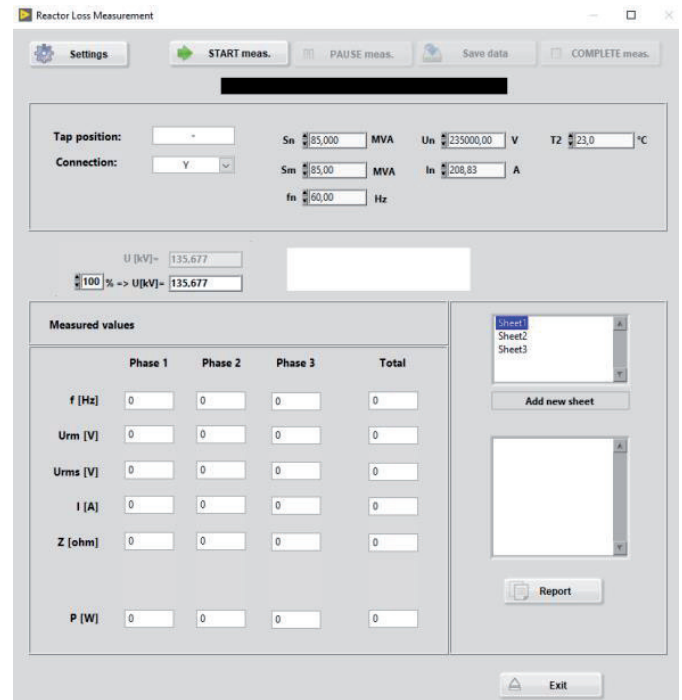


Fig. 5. Reactor Loss measurement

Based on standard requirements [1] new modules for automated measurement are developed: measurement of losses, impedance measurement, linearity test, zero impedance measurement, winding resistance measurement, temperature rise test, measurement of mutual reactance, IVPD module and control measurement. For complex measurements (losses, temperature rise test) ATT provides the possibility of subsequent data analysis.

The example for *Loss measurement* is given in Fig 5. After starting the measurement, measurements in real time from measuring bridge are displayed in ATT user interface. Test engineer decides about the moment of recording of the data. Immediately after recording, data are stored in files to be available for analysis, test reporting or as a source for research and development purposes.

## IV. CONCLUSION

ATT software covers most of electrical type and routine tests for power transformers, except the dielectric tests. Now, the software is expanded with new modules for measurement on shunt reactors – loss measurement, impedance measurement, linearity test, zero-impedance measurement, winding resistance measurement, temperature rise test and measurement of mutual reactance all in accordance with [1]. HV measuring bridge and accompanying software are intended for single- phase measurements. Single-phase measurement on three-phase shunt reactors would require special procedures and would result in time consuming measurements. Instead of such solution, ATT successfully integrates three measuring bridges in one three-phase system, to assure fast, accurate and simultaneous measurements for both single-phase and three-phase shunt reactors.

## REFERENCES

- [1] IEC 60076-6:2007, Power transformers, Part 6: Reactors
- [2] IEC 60076-2:2011-02, Power transformers, Temperature rise for liquid-immersed transformers
- [3] C. Bengtsson, K. Ryen, O. A. Rui, T. Olsson, Variable Shunt Reactors: Applications and System Aspects, CIGRE Pariz, 2014, A2-211
- [4] S. Goglia, D. Kanjković, M. Dorešić, Manufacturing and testing of variable shunt reactors 100 and 200 MVar, 7<sup>th</sup> HRO CIGRE, Šibenik, 2021., A2-05
- [5] Godec Z., Application of measurement uncertainty in transformer manufacture, 15<sup>th</sup> HRO, Cavtat, 2005., A2-07
- [6] Kuprešanin V., Godec Z., Roketinec I., Temperature rise test for oil-immersed power transformers according to new IEC and analysis of changes, 11<sup>th</sup> HRO CIGRE, Cavtat, 2013., A2-05
- [7] Rietveld, G. Meeting Ecodesign Efficiency Requirements: Ensuring Accuracy in Power Transformer Loss Tests via TLM System Calibration, 24<sup>th</sup> International Conference on Electricity Distribution, Glasgow, 2017
- [8] IEC/TS 60076-19:2013, Rules for the determination of uncertainties in the measurement of the losses in power transformers and reactors
- [9] Wide Band Power Analyzer D 6000, Operating Instructions, LEM NORMA, Edition 6E

# Numerical Calculation and Direct Measurement of Local Hot Spot Temperatures in Transformer Clamping Plates

Dino Kovačević, Mladen Marković, Damir Blažina

**Summary** — A verified multiphysics model is developed to simulate local hot spot temperatures in clamping structures. Stray field losses in clamping plates are obtained with the use of nonlinear impedance boundary condition through finite element method (FEM) while hot spot temperatures are simulated with the use of computational fluid dynamics (CFD). This multiphysics coupling is validated through direct measurements of local hot spot temperatures that were carried out with fiber optic temperature probes in real transformer. The local hot spot temperatures obtained with the simulations were in good agreement with the measured values, thus verifying overall approach and indirectly the calculation of local stray field losses.

**Keywords** — Transformer, Multiphysics, Stray Field Losses, Hot Spot Temperature, Clamping Plates, Fiber Optic Probes

## I. INTRODUCTION

Power transformers play a pivotal role in the robust functioning of electric grids, facilitating the efficient transmission of electrical energy across vast distances. As energy demands continue to rise, power transformers have evolved to meet the needs of modern electrical transmission systems. Particularly, transformers designed with high short circuit impedance have garnered attention due to their significance in grid stability and fault management. Their elevated short circuit impedance serves as a safeguard against potential disruptions caused by short circuits or faults in the electrical grid. By limiting fault currents, they mitigate the risk of cascading failures, thereby preserving the integrity of the overall grid infrastructure.

In the design stage of power transformer production, it is crucial to know stray field losses and their effects for optimum design of transformer. This knowledge is even more important for oil

immersed transformers with high short circuit impedance which results in higher stray field losses. Local temperature hot spots will appear in structural metallic components that are in direct contact with insulating liquid forming “faulted gasses”. The main concern of designing this type of transformers will be prevention of reaching temperature hotspots that could form gasses. With this type of transformers, thermal analysis of components such as clamps or tanks becomes important. Designers must know this information to choose appropriate materials such as non-magnetic steel.

In essence, this calculation requires multiphysics approach using numerical simulations. Stray field losses in clamps are calculated using Finite Element Method (FEM) while induced eddy currents have been modeled with surface impedance boundary condition [1], [2]. Temperatures will be calculated using 3-D steady-state Computational Fluid Dynamics (CFD) analysis. Since two different analyses will be used, effective coupling between them must be assured. Stray field losses calculated in FEM will be used as input losses in CFD analysis.

Calculation of losses and therefore temperatures is validated by experiment on 40 MVA 145 kV power transformer with its short circuit impedance value of 20%. Temperatures were measured with fiber optic temperature probes on multiple locations. Therefore, 5 different hotspots were measured on both internal and external side of clamps, as well as low and high voltage side of clamps.

In Section II, the overview of multiphysics approach combining electromagnetic and thermal modelling is given. Validation of the model with experimental tests is explained in Section III, while Section IV presents the comparison of the results, and finally the conclusion of the research is given in Section V.

## II. MULTIPHYSICS COUPLING (FEM & CFD)

### A. ELECTROMAGNETIC MODELING

Electromagnetic modeling was done in SimCenter Magnet 3D Time Harmonic (TH) Solver. Both linear and nonlinear TH calculation was done with clamping plate material S-235 (industrial magnetic steel) for which B-H characteristic is shown on Fig. 1. This material was also used for tank and cover plate modeling.

(Corresponding author: Dino Kovačević)

Dino Kovačević, Mladen Marković and Damir Blažina are with the Končar – Distribution and Special Transformers Inc., Zagreb, Croatia (e-mail: dino.kovacevic@koncar-dst.hr, mladen.markovic@koncar-dst.hr, damir.blazina@koncar-dst.hr)



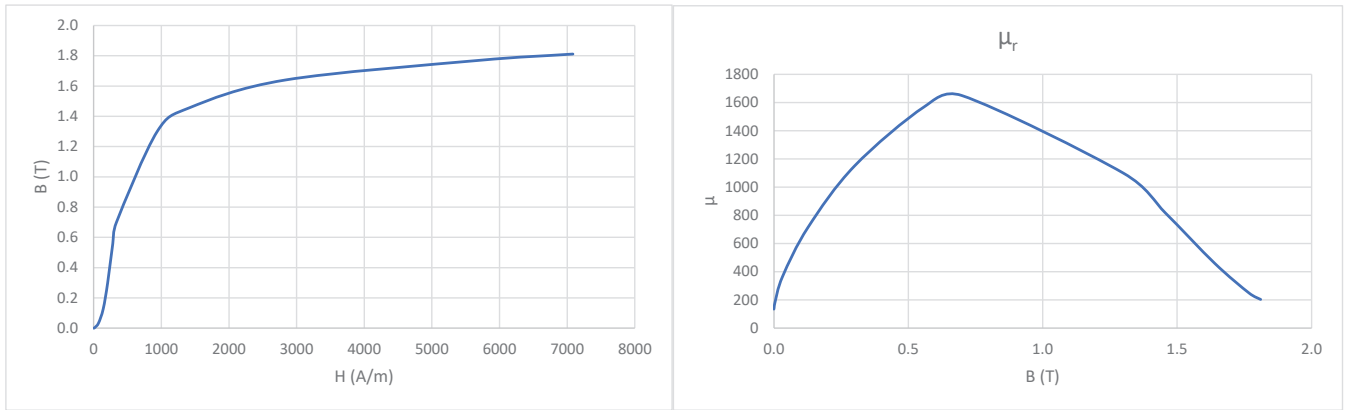


Fig. 1. Magnetic Steel Characteristic for S-235 [3]

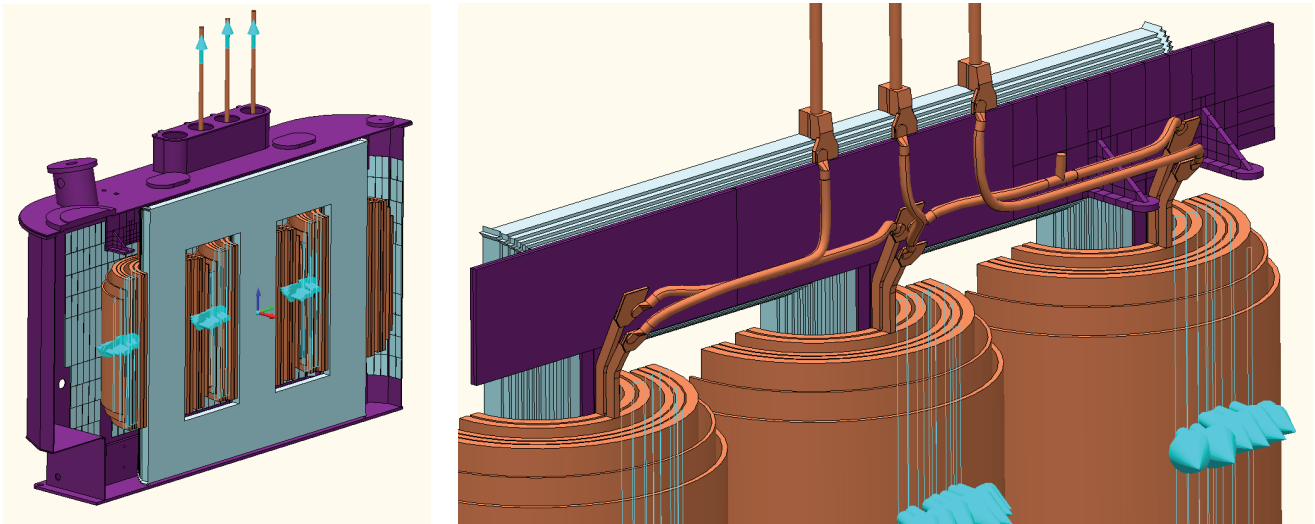


Fig. 2. LV side of modeled transformer (left) with LV star connected leads (right)

To reduce computing resources, 3D model was divided into two halves: one half for HV and the other one for LV side (computed separately), where LV side included detailed geometry of LV leads shown on Fig. 2.

Apart from dividing the transformer in two halves, further reducing of computing resources was done by using Surface Impedance boundary condition for each magnetic steel object (tank, tank plate, clamping system), even though the losses for thermal modeling were only needed to be calculated in the clamping system itself. For further notice, nonlinear solver gave approx. 15% higher loss values than linear solver but took considerably more solving time (counted in days instead of hours), so the majority of preparing calculation was done in linear solver, and the final calculation of the losses that were needed for thermal analysis were obtained by nonlinear solver.

### B. THERMAL MODELING

Thermal modeling was conducted using ANSYS CFD software package. The initial step involved preparing the model's geometry using ANSYS SpaceClaim. Clamping plates serve the purpose of pressing the core's steel sheets together horizontally, as well as pressing the windings vertically. They exist on both the upper and lower yokes. However, solely the upper clamps were modeled, given their association with hotter oil on top side of transformer. To simplify the model, certain components of clamps that were not considered important in calculation were removed or slightly changed. In the modeling process, the clamping plates were depicted as solid objects immersed within an oil domain. While components

such as the core, windings, and tank were excluded from the model, the focus remained solely on the clamping plates within the oil, Fig. 3.

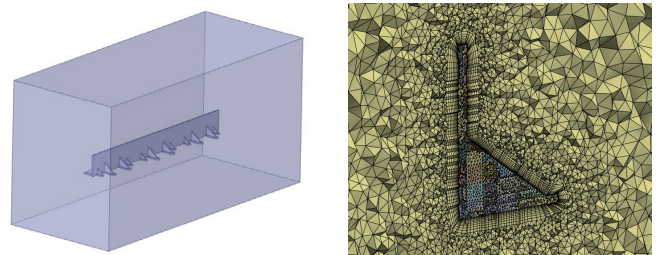


Fig. 3. Clamping plate submerged in oil domain (left) with cross sectional view of the mesh (right)

The subsequent meshing phase was executed using ANSYS Meshing software, utilizing tetrahedral elements for both solid and fluid domain. Acknowledging the significance of the boundary layer in problems involving heat transfer between solids and fluids, an inflation layer was used. With a total cell count of five million, the quality of elements was maintained to guarantee stable simulation and accurate results.

ANSYS Fluent was used to configure and solve the simulation utilizing a steady-state 3D solver. As oil enters the tank from the bottom, it gets heated by the core and windings and accelerates towards the top of the tank. At the top, oil from all sides of the tank is being mixed which makes it a reasonable assumption that flow in top of the tank is turbulent. The turbulence model chosen was

k-omega SST, which yielded satisfactory results. Material used for the clamps was steel, while the fluid domain was represented by mineral oil with thermal properties supplied by the manufacturer. Fluid's specific heat, viscosity and thermal conductivity were modelled with respect to temperature. Due to the natural convection problem, buoyancy was accounted for using the Boussinesq density model. This model assumes constant density for all equations except the gravitational term in the momentum equation. Thermal expansion coefficient was used together with constant density to ensure proper density modeling and natural driving force of oil.

Loss density data, imported from Simcenter Magnet software, were assigned to solid part of the domain. The losses from FEM analysis were applied as heat sources within the CFD analysis. Pressure boundary condition was applied to the outer boundaries of the oil domain with temperature equal to the measured top-oil results.

Residuals were considered converged under  $10^{-3}$ . To ensure simulation stability, heat imbalance, mass imbalance and  $y^+$  were monitored as well as temperature of the probes.

### III. MODEL VALIDATION

Computational model was validated by direct measurement of local hot spot temperatures using fiber optic temperature probes. 40 MVA 145 kV power transformer was chosen, having relatively high short circuit impedance of 20% for medium power transformer. Sensors were installed during the assembly phase and transformers underwent temperature testing. The recorded temperatures were then compared and used for validation.

Fiber optic temperature probes were affixed to various points on the clamping plates, chosen based on temperature results from the multiphysical model. Positioning of the probes covered both core clamps and winding clamps on low voltage and high voltage side of the transformer. Probes were placed on core clamps on both internal and external side. Eddy losses FEM analysis showed that clamps closer to tap changer will be induced by higher losses, therefore probes were placed on that side of clamping plates which is shown on Fig. 4.

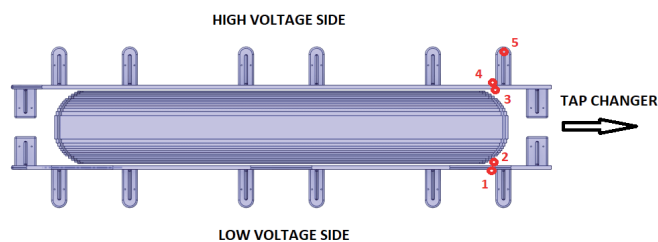


Fig. 4. Top view of clamping plates and position of the probes

Fiber optic sensors were attached to the clamping plates with a conductive adhesive as recommended by the manufacturer, shown on Fig. 5. The probes were still surrounded by the oil, however the glue ensured efficient heat transfer via thermal conduction.

Transformer was loaded up to full capacity in ONAF mode until stationary temperature was achieved, Fig. 6. Initially, it was loaded at position 15, representing the lowest voltage level (-). In that tap position, regulation windings remain unloaded, leading to a reduced short circuit impedance and lower generated losses in the clamping plates. However, overall losses in the transformer's windings and core are higher, resulting in elevated top oil temperature. Following the recording of top oil and probe temperatures, the voltage was adjusted to tap position 1, which corresponds to

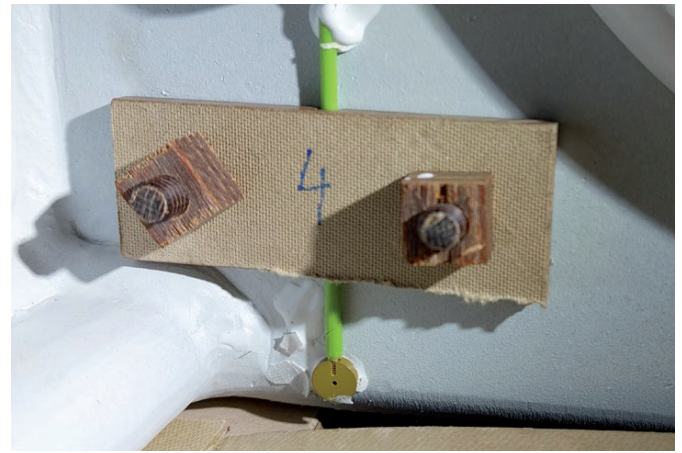


Fig. 5. Detailed view of fiber optic probes mounted on clamps

the highest voltage level (+). In this configuration, the short circuit impedance is maximized, leading to elevated losses in the clamping system, however top oil temperature will be lower. Resulting temperatures and analysis of both tap positions will be presented in subsequent chapter.



Fig. 6. Power transformer during experiment

### IV. RESULTS

Simulation results show stray field losses from FEM calculation on the left, alongside with corresponding temperature distribution obtained through CFD analysis on the right, Fig. 7. The connection point between the steel clamp and winding clamp experienced higher stray field losses, aligning with the local temperature hot-spot at that location. Many factors effect where stray field losses will be induced, but in this case, that connection turned out to have the most significant impact. Due to the steel being a good thermal conductor, temperature difference between hot and cold spots is not as large as stray field loss plot could indicate. Higher induced losses in smaller parts of the plate are being thermally conducted through the rest of the plate.

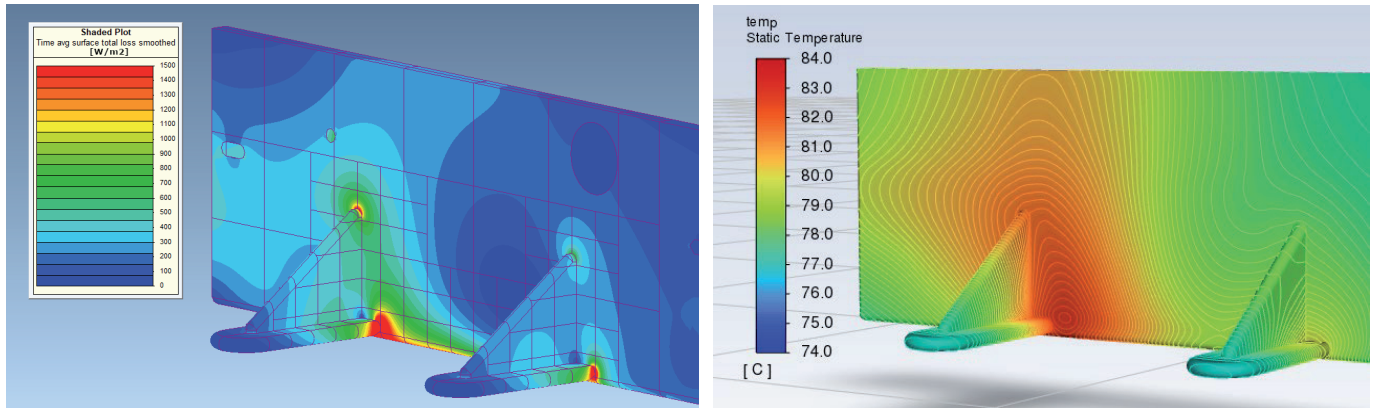


Fig. 7. Eddy losses plot (left) with corresponding temperature field (right)

Results from both simulations and experimental tests were collected and analyzed. A total of 5 probes were positioned on various places in the clamping plates as described before. Resulting comparison between measured and simulated hotspot temperatures for various positions were presented in Fig. 8. This corresponds to tap position 15.

In this scenario, the temperature rise captured by both measurements and simulations remains under 9K. Moreover, the temperature variance between measurement and simulation is not exceeding 1,6K at the worst. The least accurate positions were 1 and 2 on the low-voltage side of the clamping plates.

Moving to tap position 1 where losses induced in the clamps are highest, hotspot temperature rise will increase. Probe positions

1 and 2 that showed max. error of 1,6K were analyzed in tap position 1. Interestingly, the temperature difference between simulation and experiment remained consistent and even decreased. This realization is important, as it emphasizes that increasing the loss density in clamping plates didn't increase the error margin. Considering all the circumstances, this error is considered sufficient.

Probe position 5 shows hotspot temperature within the winding clamps. It is obvious that winding clamps pose minimal concerns for this power transformer. However, it's worth noting that in a different transformer setup, where the primary canal is located beneath the winding clamps, the risk of overheating might be more relevant.

Top oil temperature was measured 74,8°C in tap position 15 (-)

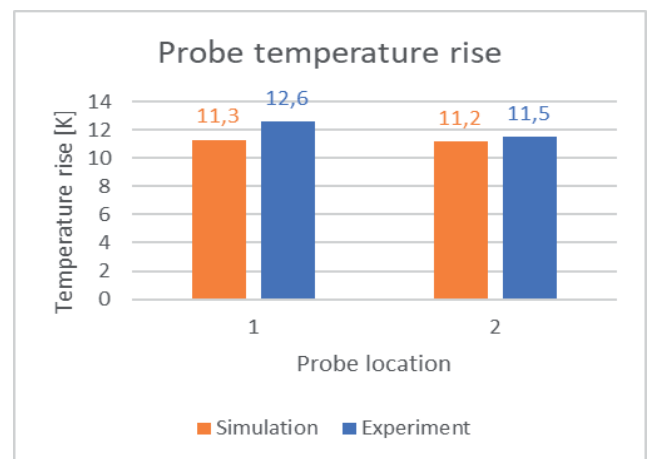
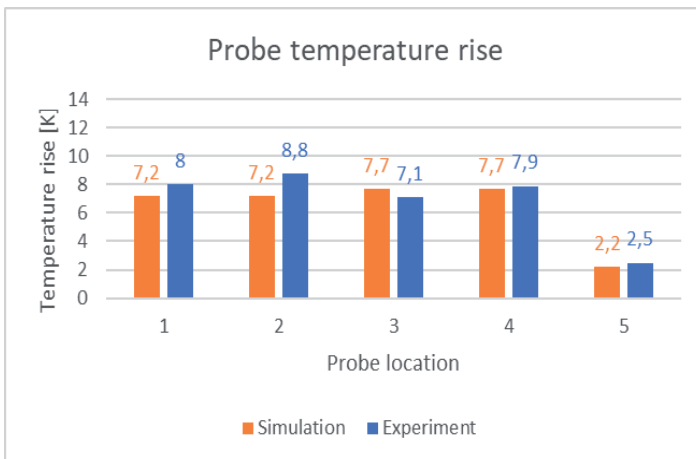


Fig. 8. Probe temperature rise in tap position 15 (left) and 1 (right)

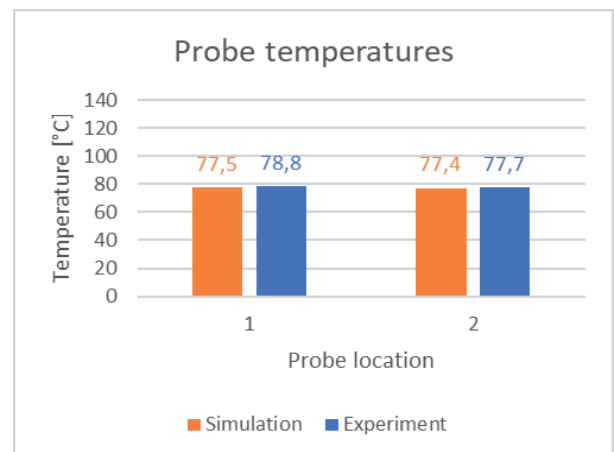
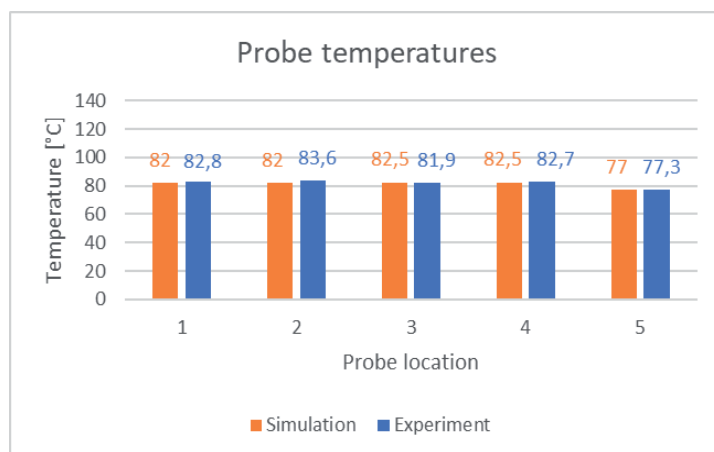


Fig. 9. Probe temperatures in tap position 15 (left) and 1 (right)

and 66,2°C in tap position I (+). Graph with probe temperatures that take top oil temperatures into account is shown on Fig. 9. For this specific power transformer, it was found that probe 2 on LV side of the internal steel clamp in tap position 15 (-) registered the highest temperature. Additionally, tap position 15 (-) consistently exhibited higher temperatures due to its elevated top-oil temperature. It's important to point out that this was the case specific for this power transformer. In other transformers with higher short circuit impedances, tap position I could potentially lead to higher hotspots.

For this particular power transformer, probe temperatures remain well below 140°C, a threshold at which the formation of gases could occur for most mineral oils.

## V. CONCLUSION

The paper presented multiphysics approach combining electromagnetic and thermal modeling. It has been shown that this methodology can be effective for analyzing local hot spot temperatures in transformer clamping plates. The validation process, which involved direct measurement of local hot spot temperatures using fiber optic temperature probes, demonstrated the accuracy and reliability of the computational model. The results from simulations aligned closely with the experimental measurements, highlighting the model's capability to predict temperature behavior with a sufficient level of precision. With an emphasis on the specific power transformer investigated in this study, it's important to recognize that results may vary for transformers with different short circuit impedances. Upcoming studies might examine power transformers with higher short circuit impedances, potentially revealing tap position I as less favorable.

## REFERENCES

- [1] D. Žarko, Z. Maljković, and S. Štefan, "Calculation of Losses in Core Clamps of Transformer Using 3-D Finite-Element Method" *Macedonian - Polish Symposium On Applied Electromagnetics*, Ohrid, Macedonia, 2006.
- [2] L. Šušnjić, Z. Haznadar, and Z. Valković, "Electromagnetic Analysis Applied to the Prediction of Stray Losses in Power Transformer" *ICEM 2004 Conference Proceeding*, Krakov, Poland, 2004.
- [3] F. Paolucci, A. Rousseau, "Passive Magnetic Shield – Steel Material", PPT presentation, ITER, 20.7.2021.

# Regression Learner Application Model-Based Short-Term Load Forecasting for Mascouche (Quebec, Canada)

Mouctar Tchakala, Tahar Tafticht, Iqbal Messaïf, Md Jahidur Rahman

**Summary** — Load forecasting is crucial for power systems optimal operation and allows power utilities to overcome technical and economic issues. Some forecasting techniques are currently being deployed on a large scale to meet the requirements of increased energy demand while balancing it with the production to achieve socio-economic benefits for sustainable development. In this paper, we are diving into the forecasting using the regression method. We are focusing on short-term load forecasting and how it can give businesses valuable insights into future sales, labor needs, and more. Power utilities use short-term load forecasting technology to make reasonable power systems. A forecasting model with low prediction errors helps reduce operating costs and risks for the operators leading to models' optimization. To make things real, we are using actual load and weather data from the Hydro-Quebec database. We will be exploring the capabilities, advantages, and limitations of this method, all while keeping an eye on the changing landscape of electricity supply and demand. Our study is centered around the Mascouche region in Quebec, Canada, where the load fluctuates between 60 to 140 megawatts.

**Keywords** — Forecast, regression, short-term load forecasting, data, optimization, power systems

## I. INTRODUCTION

In many decision-making processes, prediction plays a key role and should take into account the stochasticity in its outcome. Load forecasting is essential to maintain the balance of power supply and demand in power grids, and serves as the foundation of power market operation. Power systems planning and operation rely on accurate load forecasting on various time horizons [1]. Electricity is an essential guarantee for industrial production and social life. To meet the consumers' satisfaction and generate profit, electric power companies should balance the supply and need by scheduling a series of generators in the most efficient manner [2]. Power systems' operators need to make power generation plans in advance to achieve economical and reliable operation. The electricity demand is increasing with the economic growth. The emer-

gence of a large number of electric vehicles and various household appliances has brought more uncertainties to the management of power grids. In addition, the increase in intermittent renewable energy sources (RES) connected to the power grids, especially photovoltaic and wind turbine, makes it more challenging to manage power systems. The increased RES penetration has raised the need for spinning reserves to offset the fluctuation of RES generation [3]. These two new challenges pushed electric power companies to improve their operational capabilities. As a result, decision-makers have higher requirements for the accuracy of load forecasting.

Due to measurement errors, lack of knowledge of input data, and model approximation errors (e.g. due to imperfections in the model formulation, the estimation process, etc.), prediction uncertainty can arise. In load forecasting, the multiple linear regression method is used to seek a statistical insight into the relationship between dependent and independent variables. Regression analysis does so by using ordinary least square estimation to draw a linear relationship between load and its determinants.

In energy systems, uncertainty in the prediction of the key factors, due both to the stochasticity in the data and the approximation of the prediction models, can cause high costs to the market participants (generators, customers, etc.) when not properly accounted for. Particularly, in intermittent renewable energy integrated power systems (wind and solar PV), the impact of such a highly variable energy sources on system reliability is an important aspect that must be assessed when wind and solar power penetration is significant. Therefore, considering the high penetration of intermittent power sources in the new competitive power systems, the necessity of having access to reliable methods of power prediction has become more evident for the sustainability and efficient management of the energy market: combining accurate short-term load forecasts enables operators to commit the balance of the generation fleet to economically and securely serve future load.

This paper presents a real time case study of Mascouche region through the use of regression learner application as short-term load forecasting method. Different methodologies in load forecasting are discussed. Then performance evaluation indices are introduced and thoroughly presented. Finally, the regression method is applied to predict load using load and weather data followed by discussions that show the different errors out of Gaussian Process Regression (GPR) models found as the best tool for training the prediction model, and insights into future directions.

(Corresponding author: Tahar Tafticht)

Mouctar Tchakala, Tahar Tafticht and Md Jahidur Rahman are with the University of Québec in Abitibi-Témiscamingue (UQAT), Rouyn-Noranda, Canada (e-mails: mouctar.tchakala@uqat.ca, tahar.tafticht@uqat.ca, mdjahidur.rahman@uqat.ca)

Iqbal Messaïf is with the University of Science and Technology Houari Boumediene (USTHB), Algiers, Algeria (e-mail: imessaif@usthb.dz)

## II. MATERIALS AND METHODS

To better understand the framework of the proposed model, this section introduces the relevant methods, including two-stage forecasting model, Recurrent Neural Network (RNN), Long Short-Term Memory (LSTM), Attention Mechanism (AM), and Multi-layer Perceptron (MLP).

### A. TWO STAGE FORECASTING MODEL

The two-stage forecasting model is shown in figure 1. The proposed model consists of an LSTM-based module with the AM for multi-step forecasting and an MLP-based module for residual modification. The inputs of the sequence to sequence (seq2seq) module are over the past  $n$  hours where  $n$  is the length of the input window, including  $MoY_t$  (month of year, 1 to 12 represent January to December),  $DoW_t$  (day of week, 1 to 7 represent Monday to Sunday),  $HoD_t$  (hour of day, 0 to 23 represent 0:00~1:00 to 23:00~24:00),  $L_t$  (load), and  $T_t$  (temperature). At time  $t$ , the seq2seq module processes the input,  $X = (X_{t-n+1}, X_{t-n+2}, \dots, X_t)^T$ , where  $X_i = (MoY_i, DoW_i, HoD_i, L_i, T_i)$  and outputs the predictions of the next 24 h load demand via the fully connected (FC) layer,  $y' = (y'_{t+1}, y'_{t+2}, \dots, y'_{t+24})$  [2].

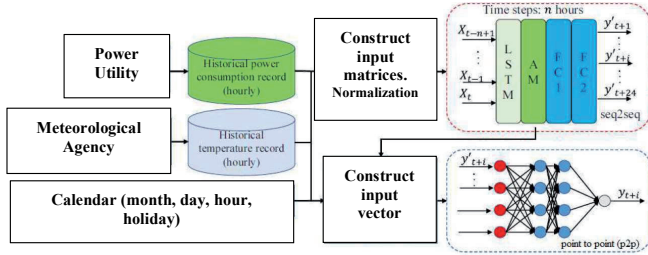


Fig. 1. The framework of the two-stage short-term load forecasting (STLF) model

### B. RECURRENT NEURAL NETWORK

The RNN is a generalization of feedforward neural network that has an internal state (i.e., memory), making it applicable to process sequences of inputs, such as speech recognition [4], natural language processing [5], and time series prediction [6], [7]. When processing a sequence of input, the RNN performs the same function for each input of data. After producing the output of current input of data, it is duplicated and sent back into the RNN as a component of the next input. Figure 2 shows the structure of a simple RNN. The mapping from the input  $X_t$  to output  $y_t$  can be described using following equations [4]:

$$h_t = f(W_{xh} \cdot X_t + W_{hh} \cdot h_{t-1}) \quad (1)$$

$$y_t = g(W_{hy} \cdot h_t) \quad (2)$$

Where  $h_t$  is the hidden state at time  $t$ ;  $W_{xh}$  are shared weight matrix at current input state, previous hidden state, and output state, respectively;  $f(\cdot)$  and  $g(\cdot)$  are the activation functions.

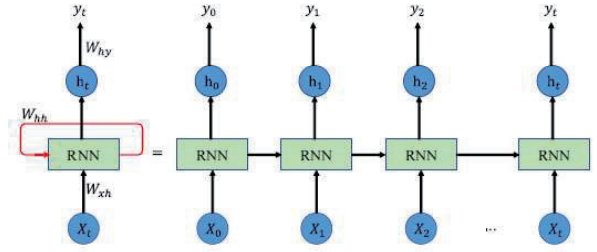


Fig. 2. The structure of a simple recurrent neural network (RNN)

Initially, the RNN takes  $X_0$  from the sequence of input and generates hidden state  $h_0$  and output  $y_0$ . In the next step,  $h_0$  and  $X_1$  are the input. The RNN repeats this process till the end of the sequence. In this way, the RNN keeps remembering the previous information. Thus, it is good at processing the sequence whose contexts are intrinsically related. However, the RNN is trained using backpropagation algorithm, and, therefore, gradient vanishing problem may occur when the sequence became very long.

### C. LONG SHORT-TERM MEMORY (LSTM)

The LSTM network is a variant of RNN, which has several gates to control the input, memory (i.e., cell state), and output, making it remembers past information more efficiently [8]. So that the gradient vanishing problem is resolved. The structure of an LSTM network is shown in Figure 3.

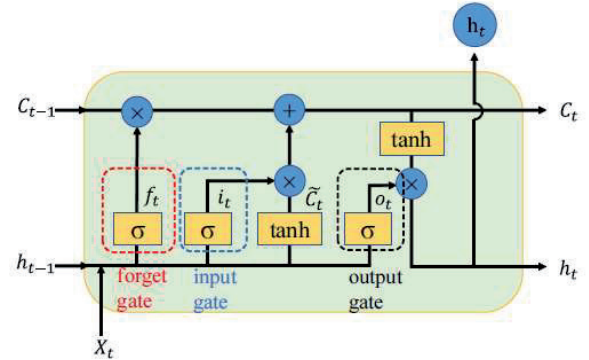


Fig. 3. The structure of long short-term memory (LSTM)

The first step in the LSTM sequence process, is to decide which information in the memory will be thrown. The decision is made by the forget gate via the sigmoid function, whose output is a value between 0 and 1. The larger the output value is, the more past information is kept in the memory. The calculation of the forget gate can be expressed as [8]:

$$f_t = \sigma(W_f \cdot [h_{t-1}, X_t] + b_f) \quad (3)$$

Where  $W_f$  and  $b_f$  are the weight matrix and bias of the forget layer,  $h_{t-1}$  is the output (i.e, hidden state) at time  $t-1$ ,  $X_t$  is the input of current state.

The next step is to determine which new information will be stored in the memory by the input gate. The tanh layer creates a candidate of the input. Meanwhile, the input gate will generate a value  $i_t$  between 0 and 1 through the sigmoid layer. The candidate,  $\check{C}_t$ , will be scaled by  $i_t$  and added to the memory to calculations of  $\check{C}_t$ ,  $i_t$ , and  $C_t$  are as follows [9]:

$$\check{C}_t = \tanh(W_c \cdot [h_{t-1}, X_t] + b_c) \quad (4)$$

$$i_t = \sigma(W_i \cdot [h_{t-1}, X_t] + b_i) \quad (5)$$

$$C_t = f_t * C_{t-1} + i_t * \check{C}_t \quad (6)$$

Where  $W_c$  and  $b_c$  are the weight matrix and bias of the tanh layer,  $W_i$  and  $b_i$  are the weight and bias of the sigmoid layer of the input gate, respectively.

Finally, the LSTM gives the output controlled by the output gate. We put the current cell state  $C_t$  through a tanh layer and multiply it by the scalar generated by the output gate.

The scalar and output of the LSTM can be computed by [9]:

$$O_t = \sigma(W_o \cdot [h_{t-1}, X_t] + b_o) \quad (7)$$

$$h_t = O_t * \tanh C_t \quad (8)$$

Where  $W_o$  and  $b_o$  are the weight and bias of the sigmoid layer of the output gate respectively.

Where  $W_c$  and  $b_c$  are the weight matrix and bias of the tanh layer,  $W_i$  and  $b_i$  are the weight and bias of the sigmoid layer of the input gate, respectively.

#### D. ATTENTION MECHANISM

The AM in Deep Learning is based on the concept of directing the focus, making the networks pay greater attention to certain factors when processing the input of data. It is used to manage and quantify the interdependence within the elements of the input sequence. Therefore, when generating the output over any time step, this layer has viewed the whole input sequence and captured the relationships between any two timeslots. [2]

A self-attention mechanism can be described as mapping a query and a set of key-value pairs to an output. The self-attention layer operates an input sequence,  $a = (a_1, a_2, \dots, a_n)$  where  $a_i \in \mathbb{R}^{d_a}$ , and generates a new sequence  $b = (b_1, b_2, \dots, b_n)$  where  $b_i \in \mathbb{R}^{d_b}$ . The query, keys, and values are computed by [33]:

$$q^i = W^q \cdot a_i \quad (9)$$

$$k^i = W^k \cdot a_i \quad (10)$$

$$v^i = W^v \cdot a_i \quad (11)$$

Where  $W^q, W^k, W^v \in \mathbb{R}^{d_a \times d_b}$  are the training parameters.

The output  $b_i$  is computed as weighted sum of a linear transformed input elements [10]:

$$b_i = \sum_{j=1}^n \alpha_{ij} (x_j W^v) \quad (12)$$

The  $\alpha_{ij}$  represents the weight coefficient between elements  $x_i$  and  $x_j$  which is computed using a softmax function [10]:

$$\alpha_{ij} = \frac{\exp e_{ij}}{\sum_{k=1}^n \exp e_{ik}} \quad (13)$$

The attention score  $e_{ij}$  can be calculated by [10]:

$$e_{ij} = \frac{(x_i W^q)(x_j W^k)^T}{\sqrt{d_b}} \quad (14)$$

#### E. MULTILAYER PERCEPTRON

The MLP is a class of feedforward Artificial Neural Networks, consisting of a series of interconnected neurons (i.e., nodes). The structure of a simple MLP network [11] with one hidden layer is shown in Figure 4. The network consists of an input layer with  $d$  units, one hidden layer with  $m$  units, and one output layer with one node. The MLP is a class of feedforward Artificial Neural Networks, consisting of a series of interconnected neurons (i.e., nodes). The structure of a simple MLP network [11] with one hidden layer is shown in Figure 4. The network consists of an input layer with  $d$  units, one hidden layer with  $m$  units, and one output layer with one node. Since MLP networks are fully connected, each node in one layer connects with a certain weight to every node in the following layer. The outcomes of the MLP can be described by Equation (15) [11].

$$y = \sum_{j=1}^m \lambda_j \cdot \psi \left( \sum_{i=1}^d w_{ij} \cdot x_i \right) \quad (15)$$

Where  $w_{ij}$  denotes the weight from  $i$ th neuron of input layer to  $j$ th neuron of hidden layer,  $\lambda_j$  denotes the weight from  $j$ th neuron of hidden layer to output layer, and  $\psi$  is the activation function. One of commonly used activation functions is the rectified linear unit (ReLU) function, which can be written as:

$$\psi(x) = \max(0, x) \quad (16)$$

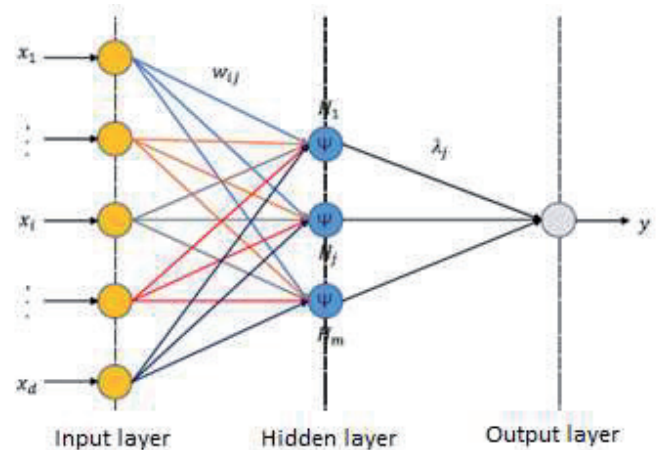


Fig. 4. A multilayer perceptron (MLP) network with one hidden layer

The MLP can approximate highly non-linear functions between the input and output without any complex mathematical formula. It has been approved that the performance of MLP in forecasting applications outperforms regression-based methods [12]. The MLP may have more than one hidden layer and multiple units in the output layer depending on different cases.

## F. ADVANTAGES AND DISADVANTAGES OF DIFFERENT MACHINE LEARNING MODELS

The advantages of linear regression include simplicity, interpretability, and fast training processes. However, this method may yield misleading results if the real relationship in the dataset is not linear. Additionally, it may be limited in expressing very complex relationships and may not model nonlinear relationships correctly. Advantages of clustering algorithms include the ability to discover structures in the dataset, better understand datasets, identify power sources with similar properties, and reveal similarities of different power sources. However, it should be noted here that these algorithms are sensitive to the data and metrics used. Additionally, in some cases it is possible to have difficulty in making a clear distinction when data points need to be separated into different groups. Advantages of artificial neural networks (ANNs) include the ability to identify and learn complex relationships, flexibility, performing well on large datasets, and scalability. Moreover, ANNs may reveal hidden patterns within data and analyze complex structures, owing to their learning ability. However, ANNs might sometimes encounter overfitting problems. This means that the network overfits the dataset and reduces generalizability. Additionally, training and configuring ANNs may require time and computational power. The advantages and disadvantages of the machine learning models discussed in this study are listed in Table I.

TABLE I.  
ADVANTAGES AND DISADVANTAGES OF ML AND ANN MODELS

Model	Advantage	Disadvantage
Linear Regression	Simple to apply, easy to interpret	It is limited to linearity, not suitable for use if there is no relationship between variables, and is sensitive to noise
Decision Tree	It is robust to independent variables, adaptable to nonlinear data, has high prediction success, can deal with categorized values, and does not need too much data	Variable to data change, unstable with noise, overfitting, not smooth or continuous, unsuitable for unstable data classes, computationally costly for large data
Support Vector Machine	Works well when separation is clear, becomes more effective as size increases, and is memory efficient	It is not suitable for large datasets; noise negatively affects the results
Efficient Linear	It is easy to apply and understand	As the number of variables increases, adaptability decreases
Gaussian Process Regression	Provides reliable intervals; suitable for uncertainty estimation	It is only for data with positive values; not suitable for data with noise
Kernel	It can capture complex and nonlinear patterns, save memory, and provide flexibility	Interpretation and explanation of the model are difficult. As feature size increases, extension becomes difficult and overfits new data
Ensemble of Trees	Good for complex and noisy problems in decision trees, adjusts variance adjustment	For multiple models, computational costs are high, and interpretation and explanation are difficult

Neural Network	It provides effective visual capability, the ability to process data even if it is not edited, and it is adaptable and offers a user interface	It has high hardware requirements, data-based operation, poor control capability, and may produce incomplete results
Long Short-Term Memory	It can capture long dependencies and handles sequential data quite well	Hardware costs are high; the dataset must be large

## G. MERIT BASED SELECTION OF THE GAUSSIAN PROCESS REGRESSION (GPR)

In this paper, we are designing a load forecasting method using data which are: (i) positive values; (ii) noiseless; and (iii) suitable for regression techniques application.

Furthermore, GPR provides reliable intervals and is suitable for uncertainty estimation which is the main concern of this paper: efficient load forecasting to reduce uncertainty in power forecasting which seriously hinders power supply through power grids and smart/mini-grids.

Based on the above, we chose to use GPR as it is clearly suitable to the technique being designed and the nature of the real-time data used.

## H. PERFORMANCE EVALUATION INDICES

The forecasted load is compared with the actual measured load for each regression model. By calculating three different statistical evaluations, the Root Mean Square Error (RMSE), the Mean Absolute Error (MAE), and the Mean Absolute Percentage Error (MAPE), the load forecasting capacity of each method and model accuracy can be assessed [13], [14].

### H.1 MEAN ABSOLUTE ERROR (MAE)

The MAE measures the average magnitude of the errors. It is calculated by:

$$MAE = \frac{\sum_{t=1}^n |Y_t - \hat{Y}_t|}{n} \quad (17)$$

Where  $\hat{Y}_t$  is the prediction,  $Y_t$  is the true value from field recording, and  $n$  is the number of measurement points.

### H.2 MEAN ABSOLUTE PERCENTAGE ERROR (MAPE)

This error percentage is a measure of the prediction accuracy of a forecasting method in statistics. It produces a measure of the relative overall fit, which can be calculated by:

$$MAPE = \frac{\sum_{t=1}^n \frac{|Y_t - \hat{Y}_t|}{Y_t}}{n} \times 100 \quad (18)$$

Where  $\hat{Y}_t$  is the prediction,  $Y_t$  is the true value from field recording, and  $n$  is the number of measurement points.



### H.3 ROOT MEAN SQUARE ERROR (RMSE)

The RMSE is the standard deviation of the residuals (prediction errors). Residuals are a measure of how far from the regression line data points are. Hence, it is a measure of how spread out these residuals are. It is calculated as follows:

$$RMSE = \sqrt{\frac{\sum_{t=1}^n (Y_t - \hat{Y}_t)^2}{n}} \quad (19)$$

Where  $\hat{Y}_t$  is the prediction,  $Y_t$  is the true value from field recording, and  $n$  is the number of measurement points.

### H.4 R-SQUARED

R-Squared is a statistical measure of how close the fitted regression line is to the results. R-squared lies between 0 and 1. Generally, the higher the R-squared value, the better the model.

The following criteria is used to evaluate load forecasting performance using the error indices:

- The RMSE is always positive and a smaller RMSE value indicates a good model.
- The R-squared lies between 0 and 1. R-Squared near 1 indicates a good model.
- The MSE is the square of the RMSE and a smaller MSE value indicates a successful model.
- The MAE is positive, similar to RMSE, and a smaller MAE value implies a successful model.
- An error percentage very close to zero means the predicted values are very relative to actual values.

## III. THE PROPOSED LOAD FORECASTING APPROACH

The procedure to implement the proposed approach is demonstrated in the following six steps:

- *Step 1: Data collection.* Two datasets need to be collected: one is load demand data; another is meteorological data.
- *Step 2: Models selection.* Some models are used in the proposed method, and suitable ones are selected.
- *Step 3: Input parameters selection.* Important input parameters such as weather parameters are evaluated and selected.
- *Step 4: Models creation and load forecasting conducted using them.* The selected ones in Step 2 will be trained and tested and then will be used to proceed.
- *Step 5: Comparison of the performance.* To compare the performance of the regression models, the forecasted load is compared with the actual measured load, and statistical error matrices are used to evaluate their accuracy.
- *Step 6: Recommendation of the ones with the highest accuracy.* Based on previous steps, the models with the highest accuracy will be selected.

The procedure is shown in the Figure 5.

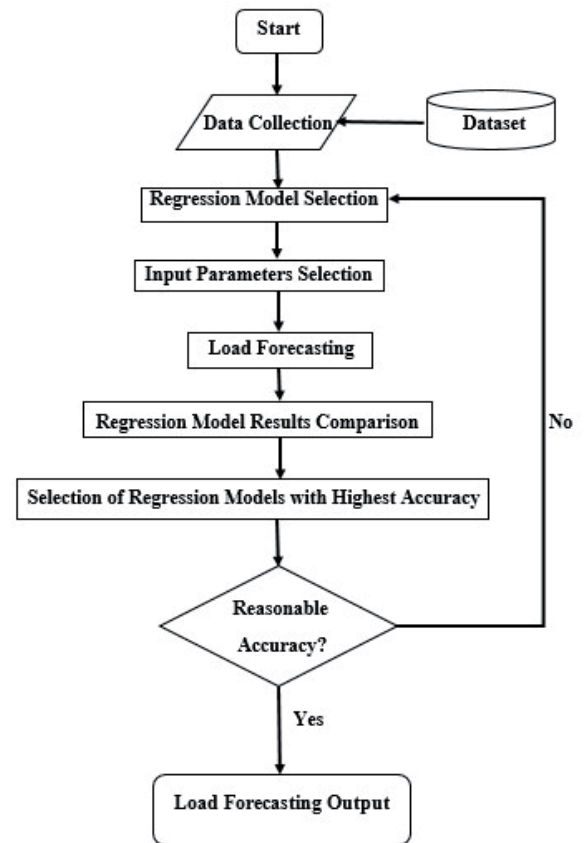


Fig. 5. The flowchart of the proposed load forecasting method

Five families of regression model algorithms provided in the Matlab regression toolbox are suitable for the short-term load prediction. They are Linear Regression, Regression Trees, Support Vector Machines (SVM), Gaussian Process Regression (GPR), and Ensemble of Trees. Table II shows these regression models. The GPR is concerned in this paper.

TABLE II.  
REGRESSION TOOLBOX

Family of regression models	Types of regression models
Gaussian Process Regression (GPR)	Rational Quadratic GPR
	Squared Exponential GPR
	Matern 5/2 GPR
	Exponential GPR
Ensemble of Trees (ET)	Boosted trees
	Bagged Trees
Support Vector Machines (SVM)	Linear SVM
	Quadratic SVM
	Cubic SVM
	Fine Gaussian SVM
	Medium Gaussian SVM
Linear Regression (LR)	Coarse Gaussian SVM
	Linear Regression Model
	Interactions Regression Model
	Robust regression model
Regression Trees (RT)	Stepwise Linear Regression Model
	Medium Tree
	Coarse Tree
	Fine Tree

#### IV. THE PROPOSED METHODOLOGY AND DATA EXPLORATION

Two files (mascouche\_1 and mascouche\_2) are provided having hourly real load in MW for two months, one month in each file having only working days, i.e., weekends are not included, and here the two months are in wintertime. Mascouche\_2, having the file (data 2), is used for training the neural network, and Mascouche\_1, having the data 1 file, is used for validating. Each of these two data files has 5 columns: Load, Days, Hours, Temperature, and the average temperature over the last five hours.

Inputs of the network are temperature ( $T$ ) and the average of the temperature ( $T_{avg}$ ), columns 4 and 5 respectively (training). The desired output (target) of the network will be the load, column 1, in MW.

The mascouche\_1 file is used for validating (testing) the neural network. It can be divided into (three days) windows, i.e., 7 windows having 3 days each:

- Windows 1: days (1, 2, and 3), Windows 2: days (4, 5 and 6).
- Windows 3: days (7, 8, and 9), Windows 4: days (10,11 and 12).
- Windows 5: days (13, 14, and 15), Windows 6: days(16, 17, and 18).
- Windows7: days (19, 20, and 21).

The purpose is that, with the temperature of the next three days, can we predict the hourly load for these three days. Comparison is using the Root Mean Squared Error (RMSE). The RMSE is the standard deviation of the residuals [15-18]. Residuals are a measure of how far from the regression line data points are, so RMSE is a measure of how spread out these residuals are. It can be calculated as follows:

$$RMSE = \sqrt{\frac{\sum_{i=1}^n (y_i - \hat{y}_i)^2}{n}} \quad (20)$$

Where  $\hat{y}_i$  is the prediction,  $y_i$  is the true value from field recording, and  $n$  is the number of measurement points.

Below are dataset details:

Data 1 is composed of five (05) columns (Load, Days, Hours, Temperature, and the average temperature over the last five hours) with 528 values each;

Data 2 is composed of five (05) columns (Load, Days, Hours, Temperature, and the average temperature over the last five hours) with 552 values each.

Dataset extent and accuracy are respectively suitable for validation and training the prediction model.

#### V. THE REGRESSION LEARNER APPLICATION

The regression learner application trains models to predict data using supervised machine learning (ML). Using this application, we can explore data, select features, specify validation schemes, train, and assess results. We can perform automated training to search for the best model type, including linear, trees, Gaussian Process (GPR), support vector machines, kernel approximation, ensembles of trees, and neural network models.

We perform supervised ML by supplying a known set of observations of inputs (predictors) and known responses. Use the ob-

servations to train a model that generates predicted responses for new input. To use the model with new data, or to learn about programmatic regression, you can export the model to the workspace or generate MATLAB code to recreate the trained model [19-21]. The below flow chart (Figure 6) shows a common workflow for training models in the Regression Learner Application.

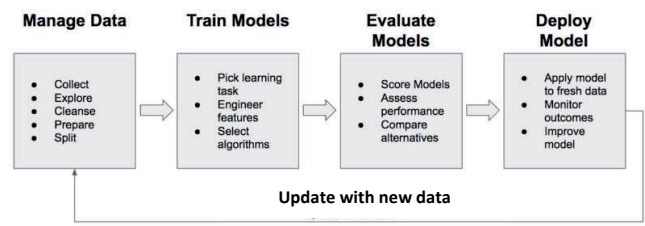


Fig. 6. Regression models training workflow

#### VI. RESULTS AND DISCUSSION

Using ML in load forecasting may significantly improve the efficiency, performance, and quality of power supply.

Below, in Table III, is shown the global simulation results:

TABLE III.

MODEL PERFORMANCES BASED ON THE MAE, MSE, R2, AND RMSE

Regression model	Performance Evaluation on Training Dataset				Prediction speed	Training time
	RMSE	R <sup>2</sup>	MSE	MAE		
GPR	2.947	0.960	8.685	2.216	~ 40 000 obs/sec	1.683 sec

The above performances table confirm the choice of the RMSE as performance indice considering the low value of R-squared (the higher the R-squared, the better); the high value of MSE; and the drawbacks of the MAE such as: (i) it doesn't penalise large errors as much as small errors, meaning that it might not reflect the true accuracy of the model; (ii) it is not differentiable at zero, meaning optimising using gradient-based methods is harder.

The use of the Regression Learner Application shows its advantages which are (i) better prediction speed, (ii) good performance, (iii) better errors estimation; and its limits such as

(i) less efficient than artificial neural networks, (ii) problem of the right choice of predictors and response for some specific data. The well-known Gaussian Process (GPR) is found as the best tool for training using the method studied with less error ( $e_{GPR} = 2.947$ ) corresponding to the Matern 5/2 type. The Table IV shows errors' values and types of GPRs. Figures. 7, 8, and 9 show predicted and actual load as well as errors of prediction between both data.

TABLE IV.

GPR MODELS AND EQUIVALENT SIMULATION ERRORS' VALUES

Model N°	GPR Type	Error Value
1.16	Squared Exponential	3.1420
1.17	Matern 5/2	2.9470
1.18	Exponential	3.6167
1.19	Rational Quadratic	2.9601

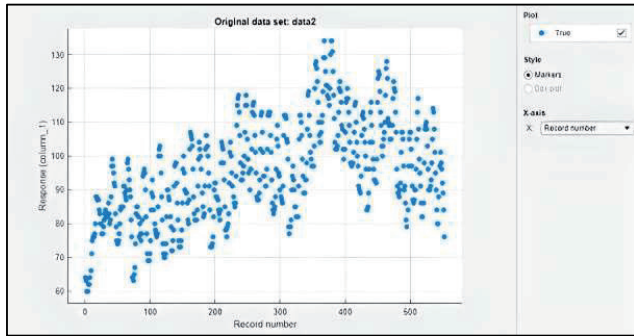


Fig. 7. Original data set with real load

Figure 7 shows the load profile with data 2 values. As indicated, the minimum load is 60 MW and the maximum load is 140 MW.

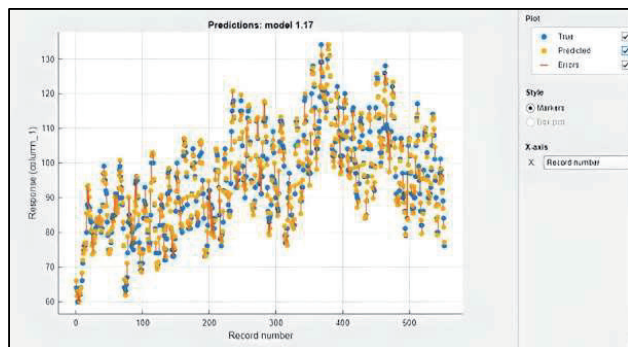


Fig. 8. Response plot

The actual load, predicted and prediction errors are plotted in the figure 8 highlighting the performance of the prediction as the similarity between actual (true) and predicted load is evidenced. In the below figure 9, only real and predicted loads are plotted without errors.

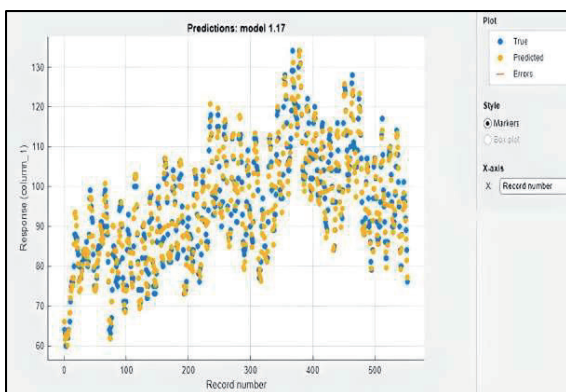


Fig. 9. Response plot without errors

The fitness graph between the actual and the predicted data by the used method is shown in Figure 10. The quality of the prediction following the distribution of the cloud of points indicates how the predicted fits with the actual data. Deviation areas along the perfect prediction line are noticeable.

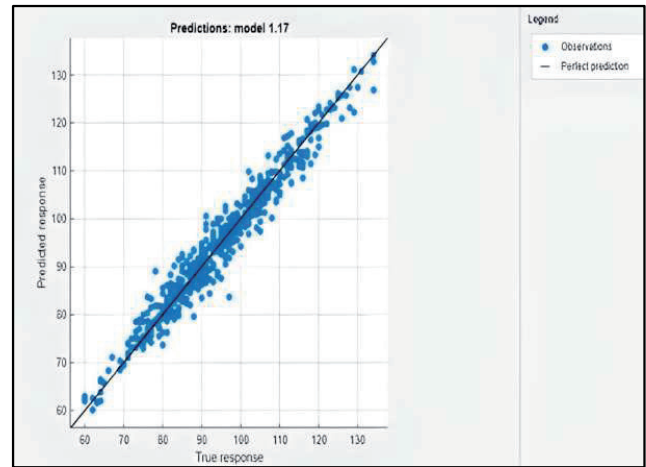


Fig. 10. Validation predicted vs. actual plot

As we strive to improve our model, we plotted the residuals. The distance from the line at zero is how bad the prediction is for that value. We remark that the majority of the points are close to the zero line which implies that the model delivers a good performance (Figure 11).

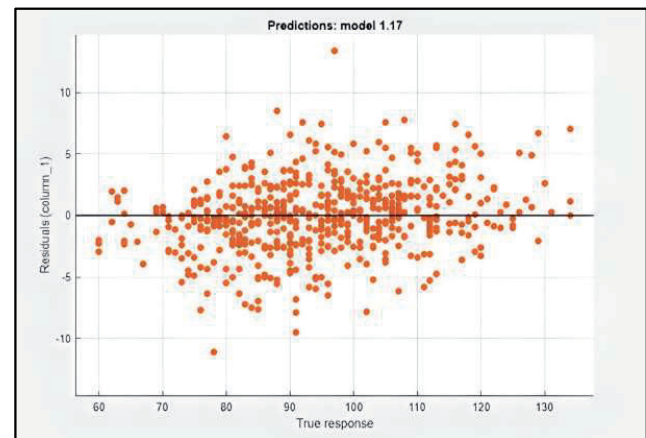


Fig. 11. Validation residuals plot for the regression model

## VII. CONCLUSION AND FUTURE TRENDS

In this study, we've applied the Regression Learner Application to forecast load using weather data. We have highlighted the advantages and limitations of this tool and showcased its capabilities without relying on load history. The recommended models are GPR, which are nonparametric kernel-based probabilistic models. Through our research, we have found that GPR is a viable methodology. It is nonparametric, meaning it is not limited to a specific function, and can calculate the probability distribution over all possible functions that fit the data. GPR is computationally efficient and provides a predictive distribution with mean values and variances. In our case, the Matern 5/2 model is recommended due to its lower error. However, the study has limitations. Hence, we're planning future works to compare and classify the best predicti-

on models and methods. Future trends that can be improved are: (i) detailed simulations with all the regression learner techniques along with comparison; (ii) optimizing data with multi-sources systems management tool (EnergyPLAN) before simulation with ML techniques; and (iii) prediction with the same data using other ML architectures such as SVM, ET, LR, and RT.

## REFERENCES

- [1] K. Chen, K. Chen, Q. Wang, Z. He, J. Hu, and J. He, Short-term load forecasting with deep residual networks. *IEEE Trans. Smart Grid*, vol. 10, no. 4, pp. 3943–3952, Jul. 2019.
- [2] Xie, Y.; Ueda, Y.; Sugiyama, M. A Two-Stage Short-Term Load Forecasting Method Using Long Short-Term Memory and Multilayer Perceptron. *Energies* 2021, 14, 5873. <https://doi.org/10.3390/en14185873>
- [3] Javadi, M.S.; Lotfi, M.; Gough, M.; Nezhad, A.E.; Santos, S.F.; Catalão, J.P.S. Optimal Spinning Reserve Allocation in Presence of Electrical Storage and Renewable Energy Sources. In Proceedings of the 2019 IEEEIC/I&CPS Europe, Genova, Italy, 11–14 June 2019; pp. 1–6.
- [4] Mikolov, T.; Kombrink, S.; Burget, L.; Cernocký, J.; Khudanpur, S. Extensions of recurrent neural network language model. In Proceedings of the 2011 IEEE International Conference on Acoustics, Speech and Signal Processing (ICASSP), Prague, Czech Republic, 22–27 May 2011; pp. 5528–5531.
- [5] Yin, W.P.; Kann, K.; Yu, M.; Schütze, H. Comparative Study of CNN and RNN for Natural Language Processing. *arXiv* 2017, arXiv: 1702.01923.
- [6] Lee, K.Y.; Cha, Y.T.; Ku, C.C. A study on neural networks for short-term load forecasting. In Proceedings of the First International Forum on Applications of Neural Networks to Power Systems, Seattle, WA, USA, 23–26 July 1991; pp. 26–30.
- [7] Lee, K.Y.; Choi, T.I.; Ku, C.C.; Park, J.H. Short-term load forecasting using diagonal recurrent neural network. In Proceedings of the Second International Forum on Applications of Neural Networks to Power Systems, Yokohama, Japan, 19–22 April 1992; pp. 227–232.
- [8] Tian, C.; Ma, J.; Zhang, C.; Zhan, P. A Deep Neural Network Model for Short-Term Load Forecast Based on Long Short-Term Memory Network and Convolutional Neural Network. *Energies* 2018, 11, 3493. [CrossRef]
- [9] David, K.; Michael, M.; Stephan, S. Short-term temperature forecasts using a convolutional neural network - An application to different weather stations in Germany. *Mach. Learn. Appl.* 2020, 2, 100007.
- [10] Shaw, P.; Uszkoreit, J.; Vaswani, A. Self-Attention with Relative Position Representations. 2018. Available online: <https://arxiv.org/pdf/1803.02155.pdf> (accessed on 5 September 2021).
- [11] Attali, J.G.; Pagès, G. Approximations of Functions by a Multilayer Perceptron: A New Approach. *Neural Netw.* 1997, 10, 1069–1081. [CrossRef]
- [12] Gardner, M.W.; Dorling, S.R. Artificial neural networks (the multilayer perceptron)—A review of applications in the atmospheric sciences. *Atmos. Environ.* 1998, 32, 2627–2636. [CrossRef]
- [13] S. García, J. Luengo, and F. Herrera, *Data Preprocessing in Data Mining*, vol. 72. Cham, Switzerland: Springer, 2015. [Online]. Available: <https://link.springer.com/book/10.1007/978-3-319-10247-4#about>
- [14] J. Han, J. Pei, and M. Kamber, *Data Mining: Concepts and Techniques*. Amsterdam, The Netherlands: Elsevier, 2011.
- [15] Mamun, A.A.; Sohel, M.; Mohammad, N.; Haque Sunny, M.S.; Dipta, D.R.; Hossain, E. A Comprehensive Review of the Load Forecasting Techniques Using Single and Hybrid Predictive Models. *IEEE Access* 2020, 8, 134911–134939
- [16] Nanae, K.; Yu, F.; Satoshi, K.; Motonari, H.; Yasuhiro, H. Sparse modeling approach for identifying the dominant factors affecting situation-dependent hourly electricity demand. *Appl. Energy* 2020, 265, 114752
- [17] David, K.; Michael, M.; Stephan, S. Short-term temperature forecasts using a convolutional neural network—An application to different weather stations in Germany. *Mach. Learn. Appl.* 2020, 2, 100007
- [18] Wang, S.X.; Wang, X.; Wang, S.M.; Wang, D. Bi-directional long short-term memory method based on attention mechanism and rolling update for short-term load forecasting. *Int. J. Electr. Power Energy Syst.* 2019, 109, 470–479
- [19] Tian, C.; Ma, J.; Zhang, C.; Zhan, P. A Deep Neural Network Model for Short-Term Load Forecast Based on Long Short-Term Memory Network and Convolutional Neural Network. *Energies* 2018, 11, 3493
- [20] Moon, J.; Kim, Y.; Son, M.; Hwang, E. Hybrid Short-Term Load Forecasting Scheme Using Random Forest and Multilayer Perceptron. *Energies* 2018, 11, 3283.
- [21] Kuo, P.H.; Huang, C.J. A High Precision Artificial Neural Networks Model for Short-Term Energy Load Forecasting. *Energies* 2018, 11, 213.



It is necessary to note that the voltages measured at the secondary side of the instrument transformer can be recalculated at primary voltages only for 50 Hz, as the voltage transfer characteristic of the instrument transformer may not be constant for the frequencies higher than 2500 Hz. To decide if the transformer has passed the test, it is necessary to check that the measured values do not exceed the long-term permissible value at which the transformer can be operated. In general, open core design instrument transformers are less prone to lead to ferroresonant behavior due to their BH characteristics, that tends to be more linear than the one of the transformers with closed core design.

### III. EMTP SIMULATION

Detailed model of the test circuit has been made in EMTP. Instrument transformers are modelled using the PI-equivalent model with nonlinear magnetizing inductance  $L_{nonl}$ , grounding capacitance  $C_3$ , primary winding resistance  $R_2$ , magnetizing resistance  $R_3$ , secondary winding resistance  $R_4$  and secondary leakage inductance  $L_2$  [5]. Nonlinear inductance is characterized using the magnetization curve obtained from measurements. Grounding capacitance is calculated in EMTP using current measurements through N and tgδ terminals during no load test. Due to open core design, end segments of transformer windings can be represented with series of equivalent parallels of capacitances and reactances, as shown in figure 3.

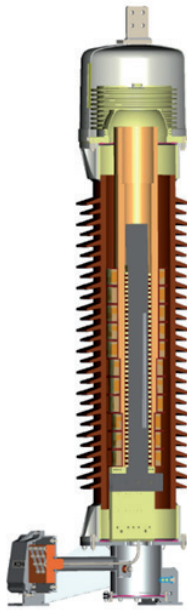


Fig. 2. Cross-section drawing of an open-core voltage transformer.

Measurement through N terminal represents current through winding segment that is closest to grounding point. Current through tgδ represents capacitance of the electrode closest to the grounding point. Nevertheless, the measured current values do not represent the exact capacitance and inductance of the transformer. It is possible to build up a “black box” model that acts as the observed transformer at its terminal, using parallel connection of equivalent capacitance and equivalent inductance. It is not necessary that the model parameters physically correspond to the real values, in this approach they are rather just mathematical representations. Therefore, the model might be considered a “black box” model. It is assumed that the initial magnetic flux of the instrument transformer is 0 Wb. During testing, the transformers are connected to source voltage for a significant time prior to circuit breaker switching off, so remanent flux can be neglected. Since there is no burden

connected to the secondary winding during tests, the primary leakage inductance is neglected. The magnetizing resistance of the open-core transformer is set to value of 100 MΩ [6]. This value is a question of future research and will be studied in more detail. The model with non-linear core magnetizing characteristics is shown in figures 3 and 4 below.

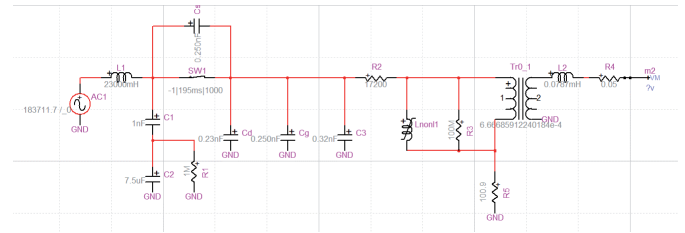


Fig. 3. EMTP model of the test circuit with circuit breaker and inductive instrument transformer models.

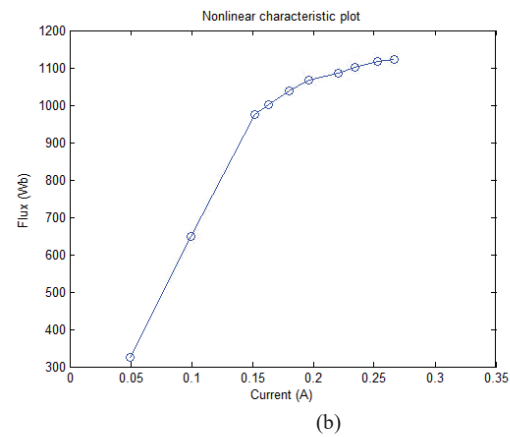
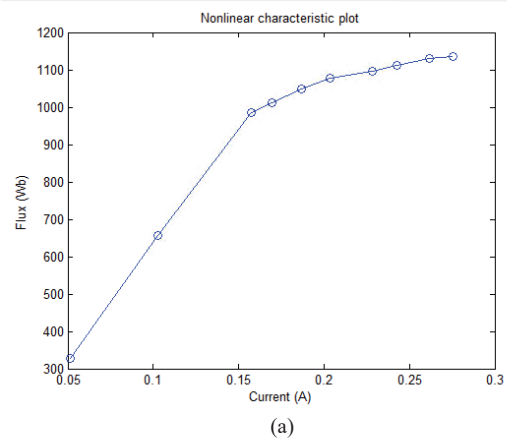


Fig. 4. EMTP model of the test circuit with circuit breaker and inductive instrument transformer models. (a) 170 kV voltage transformer and (b) 170 kV combined instrument

In the model, capacitors  $C_1$  and  $C_2$  represent capacitor divider. SW1 is an ideal switch, which is initially closed and opens at 195 ms of simulation (approximately equal to opening time in the laboratory). Capacitor  $C_d$  is added to the simulation model to simulate the grounding capacitance of the circuit breaker.  $R_5$  is a current shunt resistor for measuring the primary current, with a resistance value of 100.9 Ω. Instrument transformer parameters used in the modeling are shown in the table below.

TABLE I.  
MANUFACTURER TRANSFORMER DESIGN DETAILS

	Voltage instrument transformer	Combined instrument transformer
R2 [ $\Omega$ ]	17200	25200
R4 [ $\Omega$ ]	0.05	0.05
C3 [nF]	0.32	1.09
L2 [mH]	0.0787	52300
R0 [M $\Omega$ ]	100	100

Figures 5 – 7 show the comparison of simulated and measured response for a 170 kV inductive voltage and combined transformer. While multiple combinations of  $C_s$  and  $C_g$  were tested, to keep the paper length within reasonable limits, only a single combination was included for model verification purposes. Three values are compared versus the simulation results: voltage across circuit breaker contacts, secondary voltage of instrument transformer and primary current. Voltage across circuit breaker contacts is calculated from measured voltage at source side and voltage at primary side of the instrument transformer (calculated from measured secondary side voltage).

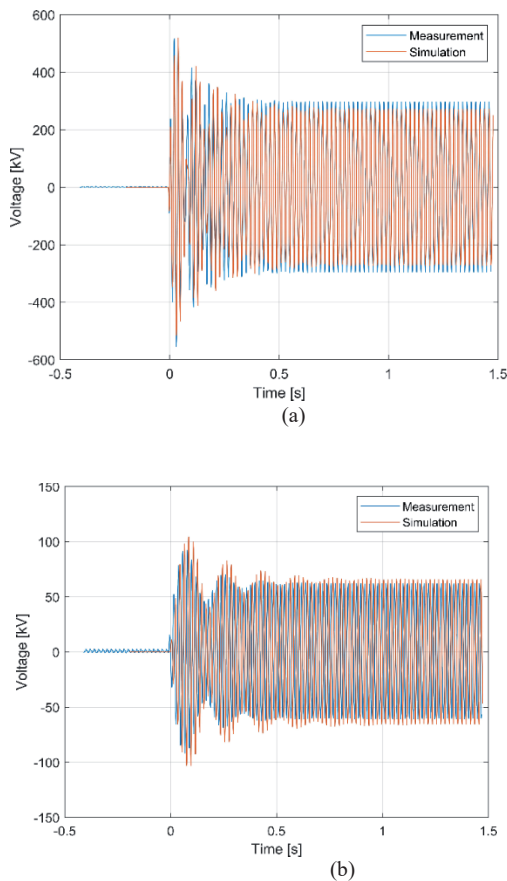


Fig. 5. Comparison of simulation and measurement results for case  $C_s=250$  pF,  $C_g=250$  pF,  $U=1.5 U_r$  (voltage across the circuit breaker contacts) for (a) 170 kV voltage transformer and (b) 170 kV combined instrument transformer

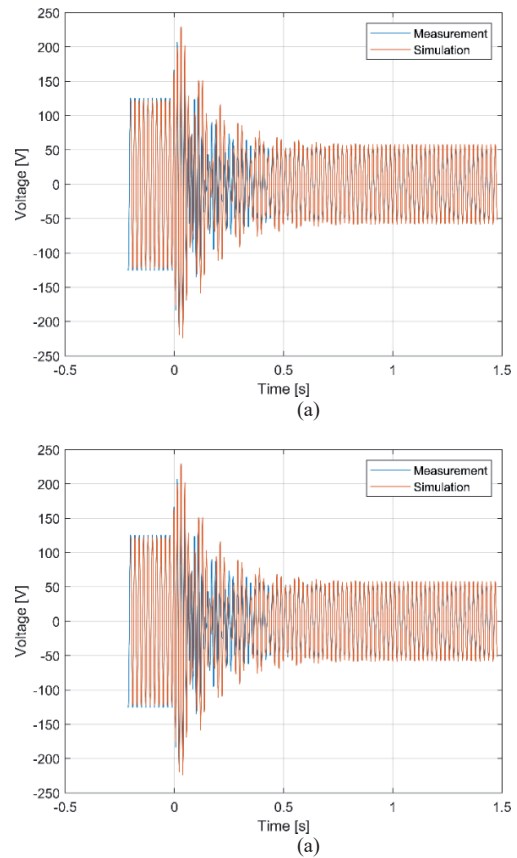


Fig. 6. Comparison of simulation and measurement results for case  $C_s=250$  pF,  $C_g=250$  pF,  $U=1.5 U_r$  (voltage across the secondary winding) for (a) 170 kV voltage transformer and (b) 170 kV combined instrument transformer

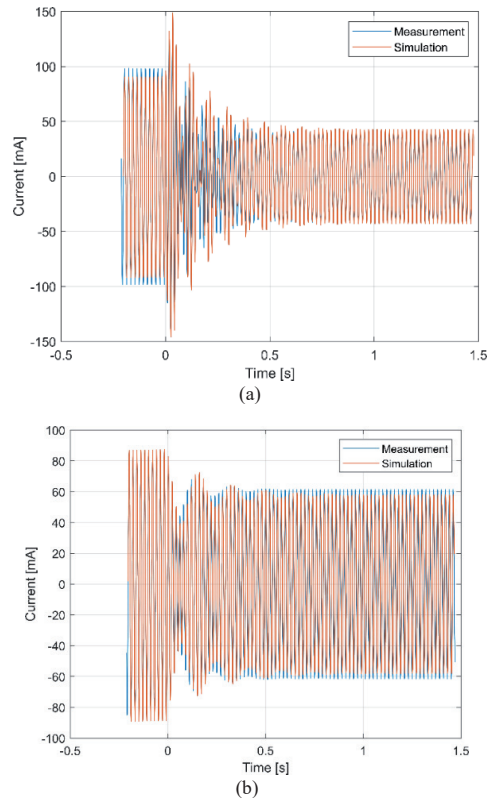


Fig. 7. Comparison of simulation and measurement results for case  $C_s=250$  pF,  $C_g=250$  pF,  $U=1.5 U_r$  (primary winding current) for (a) 170 kV voltage transformer and (b) 170 kV combined instrument transformer

From the comparison it can be seen that the results of the simulation yielded similar values and waveshapes to the measured ones. Therefore, it is possible to use such modelling to determine the possibility of resonant behavior of the observed electrical configuration. Furthermore, the singular values obtained from waveshapes in figures 5-7 are summarized in table 2. It can be clearly seen that the proposed model provided results accurate enough for engineering practices and use in further analyses. Typical errors in the observed values were under 10%.

TABLE II.  
COMPARISON OF SIMULATION AND MEASUREMENT RESULTS,  
 $C_S=250$  pF,  $C_G=250$  pF,  $U=1.5 U_R$

(a)

	170 kV voltage transformer			
	Transient measured	Transient simulated	Steady state measured	Steady state simulated
Voltage across CB [kV]	554.8	519.5	296.5	267.0
Primary current [mA]	138.4	149.0	41.5	43.3
Secondary voltage [V]	219.0	229.4	53.7	57.4

(b)

	170 kV combined instrument transformer			
	Transient measured	Transient simulated	Steady state measured	Steady state simulated
Voltage across CB [kV]	92.4	104.6	62.0	65.4
Primary current [mA]	70.8	72.7	61.5	58.2
Secondary voltage [V]	102.0	104.1	90.4	86.2

#### IV. APPLICATION ON 420 kV VOLTAGE POWER TRANSFORMER MODEL

During design phase of 420 kV voltage power transformer (VPT), proposed EMTP modelling method is used as one of the ways to confirm that power voltage transformer will not experience ferroresonance for given parameters  $C_s$  and  $C_g$ .

Figure above shows that model transformer did not experience any resonance nor ferroresonance in three EMTP simulations with different set of capacitances  $C_g$  and  $C_s$ . Primary voltage was set to 150%  $U_n$  and switching time was set to 195 ms, as it corresponds to breaker closing at zero voltage crossing that results with highest secondary transformer transient overvoltage.

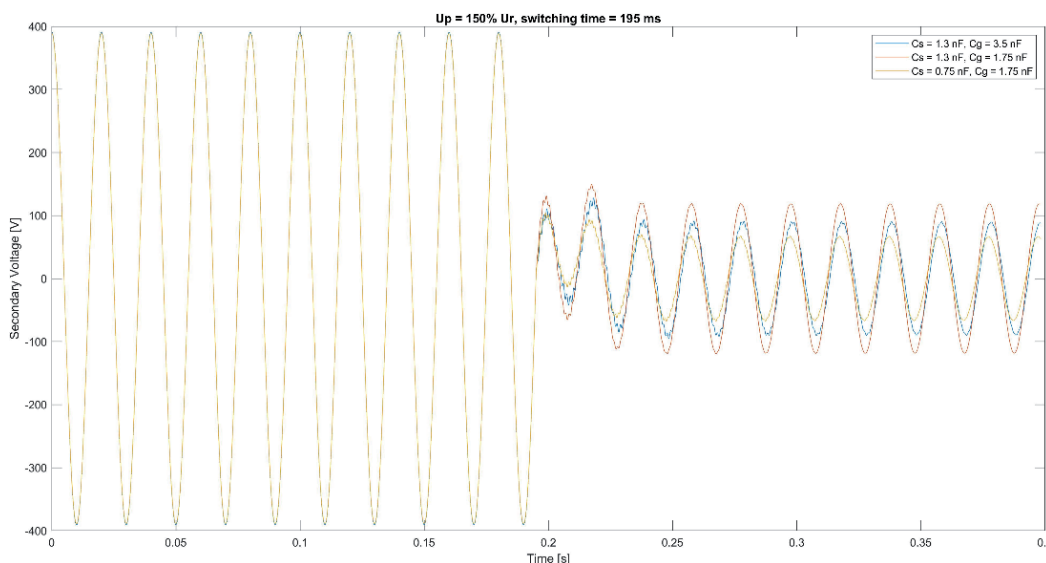


Fig. 8. Transient response of secondary voltage in ferroresonance test for different set of  $C_s$  and  $C_g$ .

Different sets of capacitances  $C_g$  and  $C_s$  lead to different stationary voltage values with open circuit breaker. With an open circuit breaker, equivalent circuit corresponds to capacitor divider with  $C_s$  as capacitance of upper branch. The lower branch of equivalent circuit capacitor divider is made from parallels of following capacitances:  $C_g$ , circuit breaker to earth capacitance and equivalent capacitance to earth of instrument transformer. In the divider lower branch has non-linear inductor of transformer open core connected to parallel with capacitance. Therefore, it is reasonable to assume that for increasing values of  $C_s$  in equivalent circuit, stationary voltage after opening the circuit breaker contacts will also increase, if no resonance nor ferroresonance occur.

#### V. CONCLUSION

The paper presents a laboratory setup designed to measure the interaction between an inductive instrument transformer and a circuit breaker. In addition to the measurements, a comprehensive EMTP model is developed to simulate the test circuit. Both the measurement and simulation results indicate that, for the specific instrument transformer units and capacitance configurations under consideration, ferroresonant behavior does not occur. The presented EMTP model proves to be effective for the analysis during the transformer's design phase. This paper offers essential guidance on testing and simulating the ferroresonant characteristics of different instrument transformers.

#### REFERENCES

- [1] Cigré WG C4.307, Resonance and Ferroresonance in Power Networks, no. February, 2014.
- [2] Valverde, V & Mazon, A.J. & Zamora, I & Buigues, G. Ferroresonance in Voltage Transformers: Analysis and Simulations. Renewable Energy and Power Quality Journal., 2011.
- [3] Jacobson, D. & Menzies, R.W. Investigation of Station Service Transformer Ferroresonance in Manitoba Hydro's 230kV Dorsey Converter Station. Proceedings of International Conference Power Systems Transients, 2001.
- [4] W. Piasecki, M. Stosur, M. Florkowski, M. Fulczyk, and B. Lewandowski, "Mitigating ferroresonance in HV inductive transformers," Int. Conf. Power Syst. Transients, IPST, vol. 9, 2009.
- [5] M. Stosur, W. PiaSecki, M. Florkowski, and M. Fulczyk, "ATP/EMTP Study of Ferroresonance Involving HV Inductive VT and Circuit Breaker Capacitance," Electr. Power Qual. Util., vol. 14, no. 2, pp. 49–52, 2008.
- [6] D. Krajtnr and I. Žiger, "Influence of HV inductive voltage transformers core design to the ferroresonance occurrence probability," Int. Conf. Power Syst. Transients, pp. 1–7, 2015.



# Several Aspects of Human Exposure to Low Frequency Fields; Incident and Internal Field Dosimetry Procedures and Related Legal Issues

Dragan Poljak, Tonko Garma, and Zorica Novakovic Šesnić

**Summary** — The paper deals with simple and efficient dosimetry procedures for human exposure to low frequency (LF) electric and magnetic fields at single and multiple frequencies, respectively. The electromagnetic interference (EMI) sources of interest are overhead power lines and transmission substations. Electric and magnetic fields due to EMI sources are either calculated or measured. Theoretical dosimetry is based on scalar potential integral equation (SPIE) for the case of the electric field assessment while the magnetic fields are computed by means of the Biot-Savart law. The internal fields in the human body are determined by using the canonical body models (disk model and cylindrical model). The obtained results are compared to exposure limits proposed by national and international legislation, respectively (National Gazette No 146/2014, 31/2019, 59/2016) and ICNIRP International Commission on Nonionizing Radiation protection). Finally, legal issues pertaining to human exposure to LF fields are addressed.

**Keywords** — Human exposure, low frequency fields electromagnetic dosimetry, legal issues.

## I. INTRODUCTION

Human exposure to low frequency (LF) fields may cause some non-thermal effects, mostly pertaining to excitable tissue [1]. Such effects are quantified in terms of electric fields induced inside the body. Prerequisites for the assessment of internal electric field is the knowledge of external fields which can be determined by calculations and/or measurements. Assessment of external fields is a task of incident field dosimetry, while internal dosimetry deals with the assessment of internal fields. [2]. Incident field dosimetry is a well-established engineering discipline and involves standard analytical/numerical approaches for the calculation of field levels and related measurement procedures. Dosimetry of internal fields is far more demanding as highly irregular geometry and heterogeneous structure of the human body must

be taken into account. Thus, the analysis within the framework of the internal field dosimetry can be carried out by using realistic, anatomically based models or simplified canonical body representations. Review of some commonly used models could be found elsewhere, e.g. in [2]. In many scenarios human being is located far enough from electromagnetic interference (EMI) source and the use of simplified canonical models is possible.

This paper is an extended version of conference papers [3, 4] and reviews some incident and internal field dosimetry procedures using simplified body models and also addresses some legal issues pertaining to the national/international legislation that proposes exposure limits.

The paper is organized, as follows; Section II deals with the incident dosimetry procedures for the assessment of external electric and magnetic fields. In addition to a most often single frequency case, a scenario involving simultaneous exposure to multiple frequencies (which is studied in somewhat lesser extent) is addressed. Typical 110 kV transmission substation as well as 110 kV overhead power line (fir tree mast) are considered as the most common LF source. In Section III internal dosimetry procedures are outlined, in particular cylindrical body model for the exposure to electric field and disk model of the torso for the exposure to magnetic fields.

Obtained illustrative results for external electric and magnetic fields and internal electric fields compared against national and international exposure limits [1, 5], respectively, are presented in Section IV.

Some legal issues pertaining to national/international legislation and proposed exposure limits are reviewed in Section V.

Finally, some concluding remarks and guidelines for future work are given.

## II. INCIDENT FIELD DOSIMETRY – THEORETICAL AND EXPERIMENTAL PROCEDURES

This section deals with computational and measurement procedures for the assessment of external electric and magnetic fields generated by LF sources. Of particular interest are power lines and transformer substations.

According to [1], for biological effects at frequencies up to 10MHz, simultaneous exposure to LF fields of multiple frequencies requires following conditions to be satisfied for external field levels:

(Corresponding author: Dragan Poljak)

Dragan Poljak is with the Department of Electronics and Computing, University of Split, HR-21000 Split, Croatia (e-mail: [Dragan.Poljak@fesb.hr](mailto:Dragan.Poljak@fesb.hr)).

Tonko Garma is with the Department of Power Engineering, University of Split, HR-21000, Split, Croatia (e-mail: [Tonko.Garma@fesb.hr](mailto:Tonko.Garma@fesb.hr)).

Zorica Novaković Šesnić is with the Croatian Transmission System Operator, HR-10000 Zagreb, Croatia (e-mail: [zorica.novakovic@hops.hr](mailto:zorica.novakovic@hops.hr)).

$$\sum_{j=1}^{10\text{MHz}} \frac{E_j}{E_{R,j}} \leq 1 \quad (1)$$

$$\sum_{j=1}^{10\text{MHz}} \frac{H_j}{H_{R,j}} \leq 1 \quad (2)$$

where:  $E_j$  and  $H_j$  is the electric and magnetic field intensity, respectively, while  $E_{R,j}$  and  $H_{R,j}$  is the reference level of the electric and magnetic field, respectively, at  $j$ -th frequency.

### A. ELECTRIC FIELD CALCULATION

Electric field in the vicinity of a wire configuration of interest is determined in two steps. First, one needs to evaluate the scalar potential around the wire structure of interest and once the potential distribution is known it is possible to obtain the electric field. The scalar potential distribution can be determined if the linear charge density over conductors is known. The linear charge density is governed by the *scalar potential integral equation* (SPIE) [2, 3]. Finally, the desired electric field distribution in the vicinity of the LF EMI source is obtained by means of the gradient operator. It is worth noting that SPIE can be solved via the Galerkin-Bubnov variant of the indirect Boundary Element Method (GB-IBEM), while the gradient operator is usually approximated by using the finite difference approximation. In particular, for the case of an arbitrary wire structure above a finitely conducting ground the impact of the ground is taken into account via the theory of images, as indicated in Fig. 1.

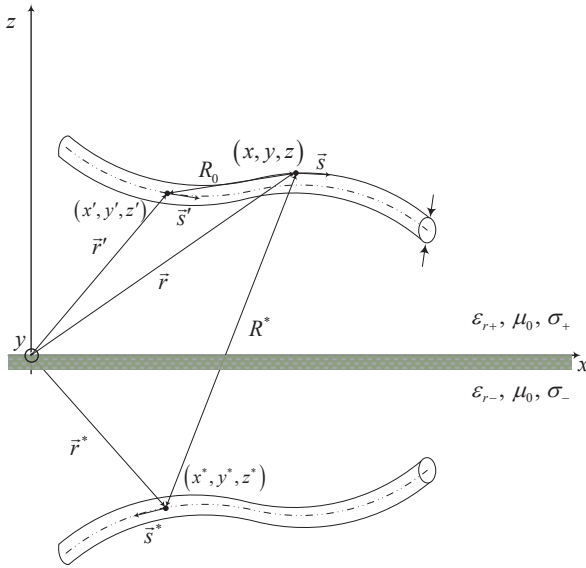


Fig. 1. Arbitrary wire configuration (The source and image wire)

It is worth noting that attenuating impact of the ground can be taken into account via corresponding reflection coefficient [5]. A general expression for a scalar potential in the vicinity of a wire configuration of length  $l$  and arbitrary shape obtained by quasi-static approximation and reflection coefficient arising from the *Modified Image Theory* is of the form

$$\varphi(\vec{r}) = \frac{1}{4\pi\epsilon_0} \int_l \left( \frac{1}{|\vec{r}-\vec{r}'|} - \Gamma_{ref}^{MIT} \frac{1}{|\vec{r}-\vec{r}^*|} \right) \rho_l(\vec{r}') ds' \quad (3)$$

Where  $\rho_l$  denotes the unknown linear charge density along the wire configuration,  $\vec{r}'$  is a radius vector of a source point,  $\vec{r}$  is a radius vector of an observation point,  $\vec{r}^*$  stands for a point at the

image source, and  $\Gamma_{ref}^{MIT}$  is a reflection coefficient arising from the modified image theory [2, 3] and is given by

$$\Gamma_{ref}^{MIT} = \frac{\epsilon_{eff}-\epsilon_0}{\epsilon_{eff}+\epsilon_0} \quad (4)$$

where  $\epsilon_{eff} = \epsilon_r - j \frac{\sigma}{\omega}$  is the complex permittivity of the ground.

Unknown linear charge density can be obtained by numerically solving corresponding SPIE [2, 3]. Provided the potential at the wire surface is known  $\varphi_l(\vec{s}')$  SPIE takes form

$$\varphi_l(\vec{s}') = \frac{1}{4\pi\epsilon_0} \int_l \left( \frac{1}{R_l} - \Gamma_{ref}^{MIT} \frac{1}{R_l^*} \right) \rho_l(\vec{r}') ds' \quad (5)$$

where  $R_l$  and  $R_l^*$  is the distance from the axis of wire in the air and image wire, respectively, to the point at the surface of the wire in the air.

As already mentioned, integral equation (5) can be numerically solved by means of GB-IBEM [6]. Once the linear charge density is known  $\rho_l$  it is possible to determine the potential in the vicinity of the wire structure. Finally, in accordance to the quasi-static approximation the corresponding electric field can be obtained as a gradient of scalar potential

$$\vec{E} = -\nabla\varphi \quad (6)$$

Equations (3) to (6) are general and valid for arbitrarily shaped wires which is of particular interest in the analysis of substation transformers [2-4]. On the other hand, if power lines with negligible sag are analyzed an approximation with straight conductors could be used and relations (3) and (5) could be simplified appreciably. Finally, the ground influence can be often neglected, as well [1]. Namely, the wire structure is assumed to be insulated in free space [1] and, consequently, the straight wire geometry of length  $2L$ , shown in Fig. 2., is considered.

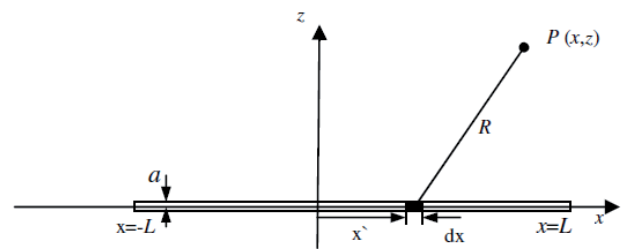


Fig. 2. Straight conductor of length  $2L$  in rectangular coordinate system

Now the Electric scalar potential in an arbitrary point  $P(x,z)$  due to a straight wire segment with linear charge density  $\rho_l$  is given by expression [1]

$$\varphi(x,z) = \frac{1}{4\pi\epsilon_0} \int_{-L}^{+L} \frac{\rho_l(x') dx'}{R} \quad (7)$$

where  $R$  is the distance from the source point at the straight wire to the arbitrary observation point  $P$ .

Provided the potential along the straight wire  $\phi_l$  is known integral expression (5) becomes an integral equation of the form

$$\varphi_l = \frac{1}{4\pi\epsilon_0} \int_{-L}^{+L} \frac{\rho_l(x') dx'}{\sqrt{(x-x')^2 + a^2}}, \quad (8)$$

where  $a$  is the wire radius.

Solving the integral equation (6) via GB-IBEM algorithm yields the linear charge density distribution along the wire configuration. Mathematical details are available elsewhere, e.g. in [1].

Once the charge density is determined it is possible to compute the scalar potential distribution in the vicinity of the wire configuration from (5). Finally, the corresponding electric field in an observation point of interest is obtained as a gradient of the scalar potential [5]:

$$E_{xi} = -\frac{\partial\varphi}{\partial x}, \quad E_{zi} = -\frac{\partial\varphi}{\partial z} \quad (9)$$

It is worth mentioning that, due to the radial symmetry, reducing the domain of interest to XZ plane can be carried out without any loss of generality.

### B. MAGNETIC FIELD CALCULATION

Calculation of LF magnetic field generated by arbitrary wire configurations is, in principle, less demanding compared to the electric field calculation, as the current flowing along the conductor configuration is known input parameter. The magnetic field of an arbitrary wire configuration is usually obtained by using Biot-Savart law for curvilinear current element, as shown in Fig 3.

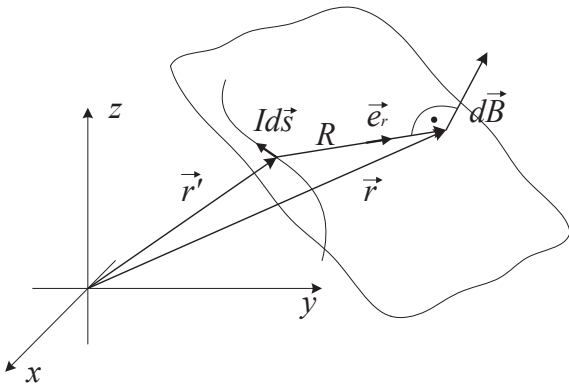


Fig. 3. Curvilinear current element

Magnetic flux density  $\vec{B}$  in an arbitrary observation point due to contribution of all infinitesimal contributions  $id\vec{s}'$  along the wire structure according to Biot-Savart law is expressed by integral

$$\vec{B} = \frac{\mu_0}{4\pi} \int_l \frac{id\vec{s}' \times (\vec{r} - \vec{r}')}{|\vec{r} - \vec{r}'|^3} = \frac{\mu_0}{4\pi} \int_l \frac{id\vec{s}' \times \vec{e}_R}{R^3} \quad (10)$$

where  $R = |\vec{r} - \vec{r}'|$  is the distance from the source to observation point, respectively.

Integral (8) can be significantly simplified if an arbitrary curved structure is considered as superposition of straight wire segments, as shown in Fig. 4.

Performing some simple mathematical manipulations  $\phi$ -component of the magnetic field generated by straight wire segment, Fig. 4., is obtained

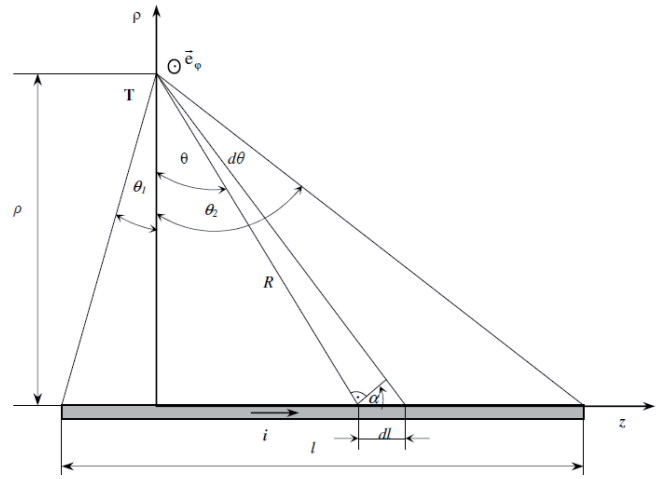


Fig. 4. Straight wire segment

$$\vec{B} = \vec{e}_\phi \frac{\mu_0 i(t)}{4\pi\rho} \int_{\theta_1}^{\theta_2} \cos\theta d\theta = \vec{e}_\phi \frac{\mu_0 i}{4\pi\rho} (\sin\theta_1 + \sin\theta_2) \quad (11)$$

where  $\rho$  is the variable of cylindrical coordinate system, while  $\theta$  is the auxiliary angle, as depicted in Fig. 4.

More mathematical details on the application of Biot-Savart law to the calculation of LF magnetic fields can be found elsewhere, e.g. in [2].

### C. ELECTRIC AND MAGNETIC FIELD MEASUREMENT

Measurements are carried out by Aaronia Spectran NF-5030 spectrum analyzer, equipped with high performance DSP and 3D magnetic- and electric-field sensor. Prior to being adjusted to detect first and higher field harmonics (up to 7<sup>th</sup>), the analyzer was placed on insulated tripod enabling adjustable measurement height. During the entire measurement process, obtained data were transferred to laptop PC for post-processing and further in-depth analysis. Typical 110 kV transmission substation as well as 110 kV overhead power line (fir tree mast), is considered, respectively, as the most common LF source for the worst case scenario, see Fig. 5.



Fig. 5. Magnetic field measurement configuration in case of 110 kV overhead power line (fir tree mast)

### III. INTERNAL DOSIMETRY PROCEDURES

This section outlines dosimetry procedures for the assessment of internal electric field induced inside the human body due to the exposure to either electric or magnetic external field, respectively.

Contrary to ICNIRP 1998 guidelines [7] in which induced current density represents the basic restriction at LF exposures in ICNIRP 2020 guidelines 2010 [1] the induced field is the basic restriction. These two quantities are simply related through the Ohm law in a differential form

$$\vec{E} = \frac{\vec{J}}{\sigma} \quad (12)$$

where  $\sigma$  is the conductivity of a tissue.

For the case of simultaneous exposure to different frequencies, as the internal field is the basic quantity up to  $f=10\text{MHz}$ , the accumulative nature of these fields is taken into account, as follows [1]

$$\sum_{j=1\text{Hz}}^{10\text{MHz}} \frac{E_j}{E_{L,j}} \leq 1 \quad (13)$$

where  $E_{i,j}$  is the internal field value at a given frequency and  $E_{L,j}$  is the assigned limit at the same frequency.

This subsection deals with simple and efficient internal dosimetry procedures for the assessment internal fields, i.e. the electric and magnetic fields induced inside the human body. Cylindrical body model is used for the exposure to axial electric field and the disk body model is used for the exposure to the magnetic field perpendicular to the body.

#### A. CYLINDRICAL BODY MODEL

When the human body is exposed to the LF electric field being axial to the body it is possible to use a simple cylindrical representation of the human being as shown in Fig. 6. Note that the body is dominantly conducting at low frequencies [8-9].

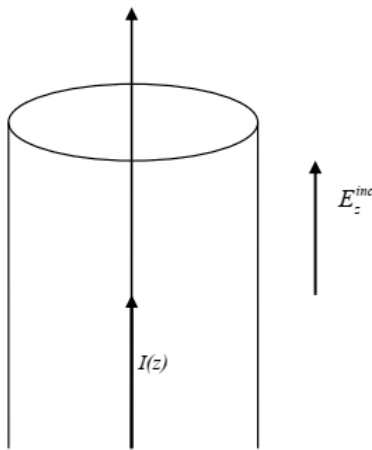


Fig. 6. Cylindrical body model

Axial current induced in the body is governed by the Pocklington integro-differential equation [2] given by

$$E_z^{inc} = -\frac{I}{4j\pi\omega\epsilon_0} \int_{-L}^L \left[ \frac{\partial^2}{\partial z'^2} + k^2 \right] g_E(z, z') I(z') dz' + Z_L(z) I(z) \quad (14)$$

where  $E_z^{inc}$  denotes the external incident field being tangential

to the finitely conducting cylinder, while  $I(z)$  is the unknown current distribution along the cylinder,  $Z_L(z)$  is the impedance per body length by which conducting properties of the body are taken into account and  $g_E(z, z')$  is exact kernel of the integro-differential equation

$$g_E(z, z') = \frac{I}{2\pi} \int_0^{2\pi} \frac{e^{jkR}}{R} d\phi \quad (15)$$

Axial current can be expressed in terms of current density

$$I = \int_S \vec{J} \cdot d\vec{S} \quad (16)$$

where  $S$  is the cylinder cross-section, while internal electric field is simply obtained from (12).

Furthermore, for the LF part of the electromagnetic spectrum the solution of equation (14) can be written in the form [2]

$$I_z(z) = j2\pi \frac{kL^2}{\psi Z_0} E_z^{inc} \left[ 1 - \left( \frac{z}{L} \right)^2 \right] \quad (17)$$

while parameter  $\psi$  is [2]

$$\psi = 2 \ln \frac{2L}{a} - 3 \quad (18)$$

where  $L$  and  $a$  stands for the cylinder length and radius, respectively.

Provided the axial current distribution is computed from (17), it is possible to calculate the related electric field magnitude by combining (12) and (16)

$$E = \frac{I_z(z)}{a^2 \pi \sigma} \quad (19)$$

Note that the accumulative field over a frequency range of interest is obtained from (13).

In this paper cylinder radius and length, respectively, is assumed to be  $a=0.14\text{m}$  and  $L=1.75\text{m}$  [2].

#### B. DISK BODY MODEL

When the human body is exposed to LF magnetic field component perpendicular to the human body, circular currents are induced inside the torso. Provided that a uniform distribution of the magnetic field at a given frequency can be assumed over the human torso a homogeneous disk model of the trunk of radius and thickness  $a$ , and constant conductivity  $\sigma$  is used [2], as shown in Fig. 7.

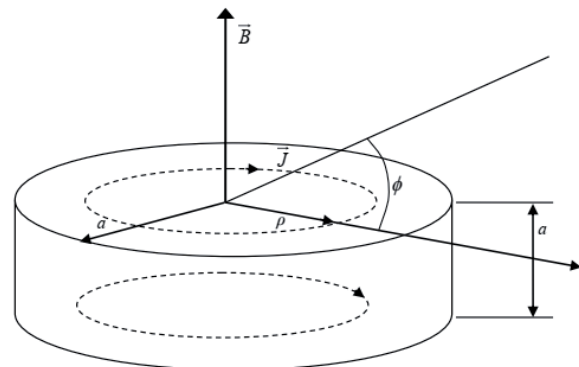


Fig. 7. Disk model of the human torso

Such a simple model is convenient as disk geometry correspond to the shape of circular current induced inside the body. This canonical geometry provides rather simple and quick assessment of the internal field starting from Maxwell equation

$$\oint_c \vec{E} d\vec{s} = - \int_s \frac{\partial \vec{B}}{\partial t} d\vec{s} \quad (20)$$

which represents integral form of Faraday law where  $\vec{E}$  stands for the circular electric field, and  $\vec{B}$  is magnetic induction perpendicular to the torso.

For time-harmonic dependence, taking into account a rotational symmetry of the disk, it follows

$$\int_0^{2\pi} E_\phi \rho d\phi = -j\omega B_z \int_0^\rho \int_0^{2\pi} \rho d\rho d\phi \quad (21)$$

and the maximal value of the circular field at  $\rho=a$  can be obtained from a simple relation

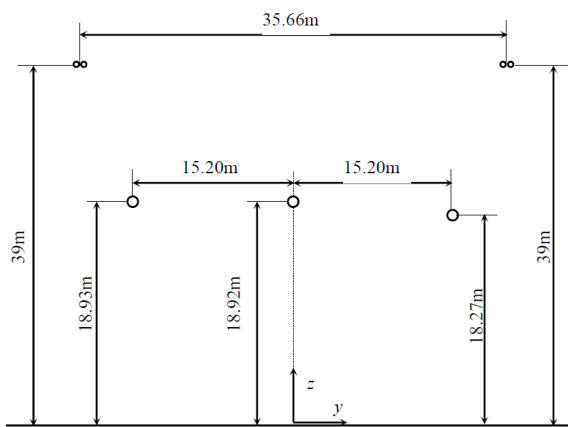
$$|E_\phi| = \pi a f \cdot B_z \quad (22)$$

Thickness of the disk is not particularly specified in literature as the total current is not quantity pertaining to basic restriction. In this paper disk radius and thickness, respectively, is assumed to be  $a=0.14$  m [8-9].

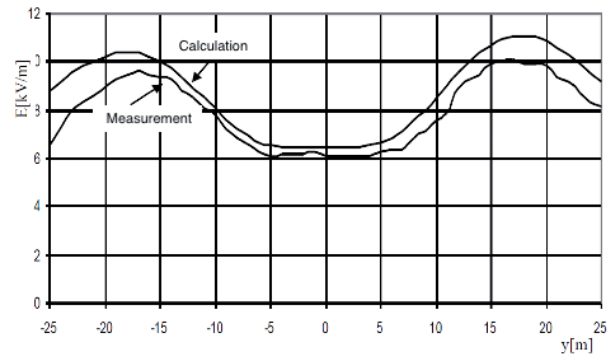
#### IV. NUMERICAL RESULTS

##### A. EXTERNAL FIELDS

First example deals with the electric field generated by 1050 kV power line composed from 3 aboveground conductors (Pittsfield, USA [10]). Figure 8.a shows the power line configuration, while our calculated results compared against measured results at height  $z=1$ m above ground are depicted in Fig.8b.



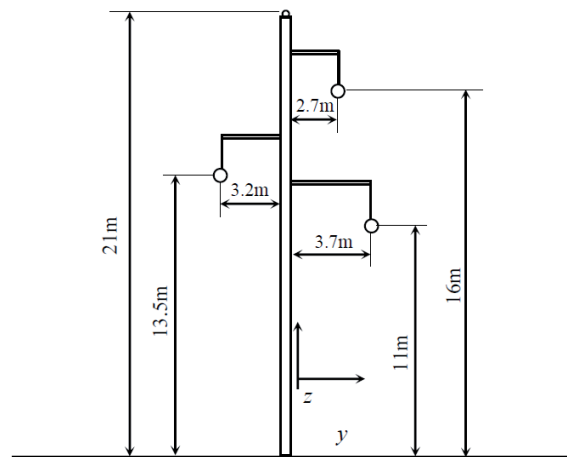
a) Geometry of 1050 kV power line



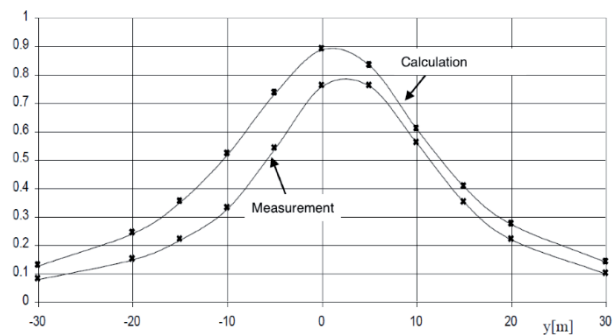
b) Calculated vs measured results at  $z=1$  m above ground

Fig. 8. Electric field from 1050kV power line

Figure 9 deals with the magnetic flux density generated by 110 kV power line consisting of 3 aboveground conductors in triangular arrangement (industrial zone near city of Split [11]). Average value of the measured current is 90 A. Figure 9a shows the actual power line configuration while Figure 9b shows the calculated vs measured results at height  $z=1$ m above ground.



a) Geometry of 110 kV power line



b) Calculated vs measured results at  $z=1$  m above ground

Fig. 9. Magnetic field from 110 kV power line

The calculated and measured results agree satisfactorily and do not exceed the reference levels proposed in [1] and [5].

Next set of Figs deals with the simultaneous human exposure to multiple frequency fields.

A view to a part of 110 kV overhead bus is shown in Fig. 10. Note that electric and magnetic field spectra are measured below this bus segment.



Fig. 10. A view to a part of 110 kV bus

Figure 11 and 12 show the spectrum of electric and magnetic field, respectively.

Observing the comparison of calculated versus measured results for the electric and magnetic fields some discrepancies can be noticed. This is mainly due to the free space approximation being used in calculation thus neglecting the reflection/absorption phenomena. The calculation of the reflected fields using the reflection coefficient approximation is likely to be carried out in a future work. Nevertheless, the simplified approach implemented in this paper provides a rapid estimation of the phenomena with useful results in an engineering sense.

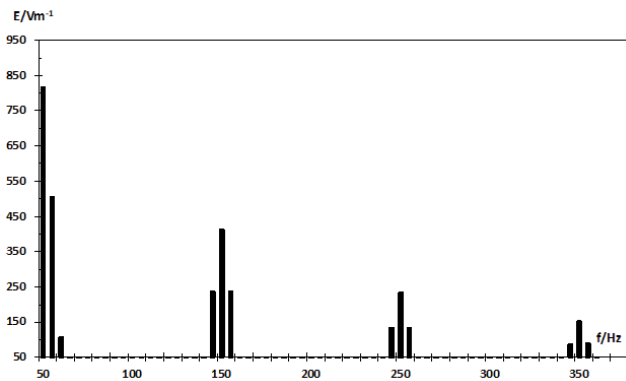


Fig. 11. Electric field spectrum

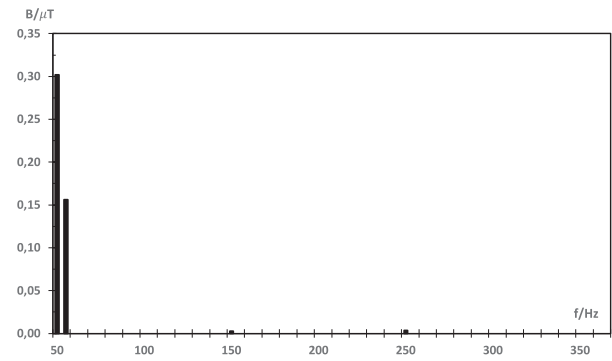


Fig. 12. Magnetic field spectrum

Furthermore, the results are postprocessed according to formulas (1) and (2). It is found that the measured electric and magnetic field values satisfy the limits expressed by conditions requested in (1) and (2).

For example, for measured magnetic induction values:  $B=0.303 \mu\text{T}$  at  $f=50 \text{ Hz}$  and  $B=0.156 \mu\text{T}$  at  $f=55 \text{ Hz}$ , taking into account condition (2) for magnetic field harmonics one obtains:

$$\frac{0302}{40} + \frac{0.156}{40} = 0.01145 \leq 1$$

Based on data provided by the equipment manufacturer, B-type measurement uncertainty is calculated for the fundamental harmonic. The obtained value taking into account confidence interval of 99.7 % ( $k=3$ ) is 42.9 V/m and 0.02  $\mu\text{T}$  for electric field and magnetic flux density, respectively. Note that the reference level for general population according to [5]  $B_{lim}=40\mu\text{T}$ .

Considering the aforementioned value for the magnetic field density and corresponding measurement uncertainty, experimental result is significantly lower than reference level. Similar reasoning may be applied in case of the electric field.

## B. INTERNAL FIELDS

Internal fields are determined using canonical models of the human body (cylindrical and disk model) taking into account all field harmonics having significant values.

For example, for measured value of electric field:  $E=815 \text{ V/m}$  at  $f=50 \text{ Hz}$ , the maximal value of the electric induced in the cylindrical body model, as a basic restriction quantity is  $E^{ind}=0.426 \text{ mV/m}$ . Note that basic restriction according to [1] is  $E_{lim}=0.1 \text{ V/m}$  which is couple of order of magnitude higher value.

Furthermore, for measured values of magnetic induction:  $B=0.303 \mu\text{T}$  at  $f=50 \text{ Hz}$  and  $B=0.156 \mu\text{T}$  at  $f=55 \text{ Hz}$ , the internal electric field, as a basic restriction quantity, is calculated by means of (19), and applying the condition (13) it follows:

$$3.14 \times 0.14 \times \left( \frac{50 \times 0.302}{0.1} + \frac{55 \times 0.156}{0.1} \right) = 1.041 \times 10^{-4} \leq 1$$

Again, for the basic restriction  $E_{lim}=0.1 \text{ V/m}$ , it is obvious that condition (13) is satisfied.

## V. LEGAL ISSUES

### A. HISTORICAL OVERVIEW OF ORGANIZATIONS DEALING WITH PROTECTION OF HUMAN BEINGS FROM EXPOSURE TO LOW – FREQUENCY ELECTRIC AND MAGNETIC FIELDS

Along with the development of the technology, there has been an increasing public concern regarding the exposure of human beings to non-ionizing radiation and possible adverse health effects. International Radiation Protection Association (IRPA) published guidelines on protection of humans from electromagnetic radiation decades ago. Guidelines based on scientific knowledge regarding the short-term exposure of humans to non-ionizing radiation, while warning in cases where risks and biological effects of long-term exposure are recognized, other measures should be taken to avoid or reduce risks [12].

In 1992, ICNIRP was established as an independent body, separated from IRPA, with a sole scientific mission to work on protection from non-ionizing radiation, continuously collaborating with international research organizations, as well as universities and other academic institutions. ICNIRP has been producing several publications such as guidelines, statements, reviews, proceedings, and notes. These publications should be regarded as strictly non-binding scientific opinions formulated into documents and by no means opinions that any country is obliged to implement into a national legislation [13]. It is worth noting that ICNIRP has established four standard committees covering: epidemiology, medicine and biology, physics and engineering, and biological aspects of radiation. ICNIRP's international membership includes individual experts covering areas such as medicine, biology, epidemiology, physics, and engineering.

### B. A REVIEW OF GUIDELINES FOR LIMITING EXPOSURE TO LOW FREQUENCY ELECTRIC AND MAGNETIC FIELDS

It is important to emphasize that EU member states apply international guidelines and recommendations arising from research findings, aiming to protect humans from possible adverse effects of non-ionizing radiation.

This paper focuses on the ICNIRP 2010 guidelines pertaining to for limiting exposure to LF electric and magnetic fields [1].

The procedure for establishing these guidelines involves several steps: identification of scientific data on effects of exposure to the fields at the relevant frequency range (laboratory and epidemiological studies); detection of considered effects with respect to possible health risk based on a proper scientific explanation; setting the minimum levels of exposure to the subject frequency range that cause harmful effects; consideration of the scientific basis related to establishing the causal relationship between the subject frequency range and diseases in humans; gathering data arising from direct interaction of fields with the human body and indirect interactions arising from contact currents.

The main objective intended to be achieved is to establish guidelines for limiting exposures to electric and magnetic fields, thus providing the protection against known harmful health effects. These guidelines are based on the evidences of thermal, neuropsychological, and reproductive effects of electric and magnetic fields on health. One of the purposes of issuing such guidelines is to provide protection to both occupational and general populations and are based on the ICNIRP 1998 guidelines [7]. The guidelines concern limiting exposure to non-ionizing radiation in order to protect against known adverse health effect on human beings.

The guidelines are based on currently available scientific knowledge and data, regardless of short-term or long-term exposures, age, or health status, and the biophysical mechanism.

Since the guidelines are not legally binding documents and, as emphasized by ICNIRP, they are based on scientific research, each country decides on the adoption of the guidelines into its legislation, considering other factors as well. Therefore, the guidelines are not implemented in the same way throughout the countries. For example, Japan and Germany have adopted the 2010 guidelines [14] which are also incorporated into their national legislation, while among other countries, Singapore, Brazil, South Africa, Croatia, and Greece fully or partially apply the 1998 guidelines [15].

In addition to the mentioned differences in defining the basic restrictions in the ICNIRP guidelines from 1998 and 2010, there are also some differences in reference levels. Table 1 shows a comparison of reference values for occupational and general populations, respectively, according to the ICNIRP 1998 and ICNIRP 2010 guidelines.

TABLE I

COMPARISON OF REFERENCE LEVELS FOR THE OCCUPATIONAL (GENERAL) POPULATION AT 50Hz

	Electric field (kV/m)	Magnetic field (A/m)	Magnetic induction ( $\mu$ T)
ICNIRP (1998)	10 (5)	400 (80)	500 (100)
ICNIRP (2010)	10 (5)	800 (160)	1000 (200)

It is evident from Table 1 that the reference levels for electric field exposure for the occupational and general population, respectively at a frequency of 50 Hz have not changed, while the reference levels for exposure of the occupational and general populations to magnetic field, i.e., magnetic induction, have doubled.

### C. PRECAUTIONARY > MEASURES/PREVENTIVE MEASURES

It is necessary to emphasize that member states of the European Union (EU) face challenges in determining the level of exposure protection due to potential scientifically unconfirmed adverse health effects resulting from exposure to fields generated by forthcoming technology systems. Also, this is due to the fact that scientific research, intrusions into human rights, industry interests, and environmental preservation should be taken into account. An overview of exposure limits for the general population of EU member states is depicted in Fig. 13.

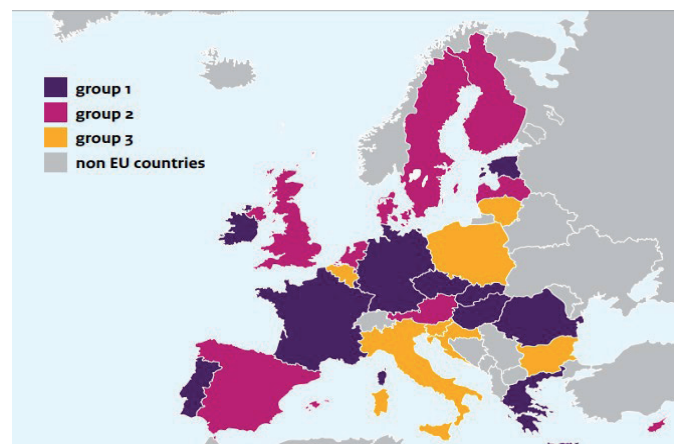


Fig. 13. Overview of exposure limits for the general population to low-frequency fields in the EU [16]: Group 1 (purple): legal limitations derived from EU recommendation- preventive policy in some countries; Group 2 (pink): no legal limitations or less strict limitations than the EU recommendation-preventive policy in some countries; Group 3 (yellow): higher limitations than the EU recommendation.

EU member states from Group 1 have adopted the ICNIRP guidelines and have implemented them into their national legislation, which means they adhere to the exposure limits determined by basic restrictions (depending on frequency, the physical quantities on which basic restrictions are based include: magnetic flux density (B), current density (J), specific absorption rate (SAR), power density (S), and internal (induced) electric field (V/m)). Some of the member states from Group 1 are: Czech Republic, France, Greece, Hungary.

EU member states from Group 2 have prescribed limitations lower than those specified by the ICNIRP guidelines and have implemented certain policies for the protection from electric and magnetic fields. Some of the member states from Group 2 are: United Kingdom (which has since ceased to be an EU member), Spain [17].

EU member states from Group 3 have established higher exposure limits than those recommended in the ICNIRP guidelines, taking into account the precautionary principle. These higher reference levels are often applied as actual exposure limits that must not be exceeded. Some of the member states from Group 3 are: Croatia, Italy, Slovenia.

In order to account for precautionary/preventive measures, the governments of member states recommend and adopt policies and principles to limit exposure to electric and magnetic fields, including:

- By applying the precautionary principle to protect people from potential harm due to exposure to electric and magnetic fields, construction of new kindergartens and schools are only allowed if they are located outside zones where the exposure to magnetic fields averaged over one year exceeds  $0.4\mu\text{T}$  (e.g. Croatia, Belgium);
- By applying the principle of limiting exposure to non-ionizing radiation establishing an upper limit for permissible human exposure to non-ionizing radiation and reducing the level of non-ionizing radiation as low as technically, economically and reasonably feasible, following the ALARA principle (As Low As Reasonably Achievable). Germany, for example, applies this principle in the vicinity of schools, kindergartens, and children's playgrounds.
- By limiting the exposure of the general population to magnetic fields, for instance, through the construction of power lines in locations distant from kindergartens, schools, and residential areas (France, Luxembourg);
- By introducing a legal obligation to measure electromagnetic fields near power lines in urban areas, with a note that citizens can request the measurement results (France);
- By introducing an obligation, during the construction of electromagnetic networks, for an environmental impact assessment study to be aligned with a maximum magnetic flux density of  $1\mu\text{T}$  (Austria);
- By raising awareness through educating the general population and publishing advice, for example, on how to reduce exposure to electromagnetic fields from mobile phones by limiting talk time, using headphones (Austria, Belgium, Cyprus, Netherlands, etc.)

World Health Organization (WHO) considers the precautionary principle as the foundation of a risk assessment when determining protective measures against non-ionizing radiation. These measures should be proportional to the chosen level of protection and non-discriminatory in application; aligned with state-of-the-art of research findings in the area; and designed to enable a comprehensive risk assessment [18].

#### *D. FINAL CONSIDERATIONS ON THE LEGAL ASPECTS OF PROTECTION AGAINST EXPOSURE TO LOW-FREQUENCY ELECTRIC AND MAGNETIC FIELDS*

The presence of electromagnetic fields in the environment and their potentially harmful impact on health of humans arouses persistent scientific, technical, and often public interest. In urban environments, it is common for numerous power engineering facilities (transformer substations, power lines) to be located in close proximity to family homes, residential areas, or workplaces.

Consequently, EU member states use various mechanisms to protect people from potential harmful effects of exposure to LF fields.

The member states are generally in charge for the implementation of the EU law. By legal acts, guidelines, and scientific opinions within the EU, it is recommended that member states, when enacting regulations, adhere to recommended exposure limits or, if deemed necessary, may prescribe higher limits. Since the Republic of Croatia is a member of the EU, the EU law has become part of its legal framework upon accession [19].

The Republic of Croatia, by enacting legal acts in the aforementioned area, participates in shaping the common EU policies. The increasing exposure of humans to non-ionizing radiation poses challenges for the Republic of Croatia, including: the proliferation of non-ionizing radiation sources in the human environment encountered by both the occupational and general population. The continuous progressive development of new technologies, which requires the use of new devices and higher frequencies; adaptation and amendment of legislation due to technological advancements by adopting new regulations or implementing various opinions of international organizations, EU directives into the legislation of the Republic of Croatia.

In the Republic of Croatia, the Law on Protection from Non-Ionizing Radiation is currently in force [17]. The principle of precaution, recommended to Member States by European Union legal acts, has been incorporated into the aforementioned law of the Republic of Croatia. Currently, in the Republic of Croatia, the Regulation on Protection from Electromagnetic Fields is also in force [5]. The Republic of Croatia, as a Member State, has determined through the Regulation, by applying the precautionary principle that the limit values of reference quantities are reduced in relation to their corresponding basic restrictions. The relevance and significance of the mentioned Law and Regulation are indicated primarily by the interest of various groups in the topic, including industry, public authorities, citizen associations, and individual citizens. However, considering a rapid development of technologies, updates and changes to existing regulations are necessary.

Note that scientific opinions presented in ICNIRP by no means bind member states to apply them as they are not legal norms contained in the EU Treaties or derived from them. Nevertheless, besides member states, other non-EU countries have decided to apply these guidelines and have incorporated them into their legislation, thereby enabling all citizens of those countries to exercise the rights arising from legal acts. By enacting the Law on protection against non-ionizing radiation as well as the Regulation on protection against electromagnetic fields [17], the Republic of Croatia has opted for further lowering the values of the recommended ICNIRP limits and, consequently, for a responsible approach to preventing potential negative effects of non-ionizing radiation.



## V. CONCLUSION

The paper deals with several aspects of human exposure to LF electric and magnetic fields dealing with incident and internal dosimetry procedures and related legal issues pertaining to radiation protection. Exposure to LF fields at single and multiple frequencies are of interest. Typical 110 kV transmission substation as well as 110 kV overhead power line (fir tree mast), is considered as the most common LF source. Note that the measured fields pertain to the worst case scenario, i.e. to the fields below tubular busbar within the substation. Furthermore, the measured results are postprocessed and, finally, internal fields are determined by using the canonical body models (disk model and cylindrical model). The obtained results are compared against reference levels proposed by Croatian regulations for the protection from electromagnetic fields (National Gazette No 146/2014, 31/2019) and ICNIRP (International Commission on Nonionizing Radiation protection) Guidelines 2010.

Future work is likely to deal with several aspects of human exposure to high frequency (HF) fields.

## REFERENCES

- [1] ICNIRP Guidelines for Limiting Exposure to Time-varying Electric and Magnetic Fields (1Hz–100kHz), *Health Physics* 99(6):818–836; 2010.
- [2] D. Poljak, M. Cvetkovic, *Human Interaction with Electromagnetic Fields*, St. Louis, USA: Elsevier, Academic Press, 2019.
- [3] D. Poljak, Z. Novakovic Sesnic, “Human Exposure to Low Frequency fields – Incident Field Dosimetry and Review of Related National and European Legal Acts”, (in *Croatian*), Proc HRO-CIGRE, Sibenik, Croatia, Nov. 2021.
- [4] D. Poljak et al., “Simultaneous Exposure of Humans to Fields of Different Frequency – Incident and Internal Field Dosimetry with Respect to National and International Legal Acts”, (in *Croatian*), Proc HRO-CIGRE, Sibenik, Croatia, Nov. 2023.
- [5] Regulation on Protection from Electromagnetic Fields (Official Gazette 146/2014, 59/2016, 31/2019) (in *Croatian*)
- [6] D. Poljak, K. El Khamlichi Drissi, *Computational Methods in Electromagnetic Compatibility: Antenna Theory Approach versus Transmission Line Models*, Hoboken, New Jersey: John Wiley & Sons, 2018.
- [7] ICNIRP Guidelines for Limiting Exposure to Time-varying Electric, Magnetic and Electromagnetic Fields (up to 300 GHz), *Health Physics* 74(4):494–522; 1998.
- [8] King, R.W.P., Sandler, S.S., “Electric Fields and Currents Induced in Organs of the Human body When Exposed to ELF and VLF Electromagnetic Fields”, *Radio Sci.*, Vol. 31, pp. 1153–1167, Sept.–Oct. 1996.
- [9] King, R.W.P., “Fields and Currents in the Organs of the Human Body When Exposed to Power Lines and VLF Transmitters”, *IEEE Trans. Biomed. Eng.*, Vol. 45, No 4, pp. 520–530, April 1998.
- [10] J.E.T. Villas, F.C. Maia, D. Mukhedkar, V.S. Da Costa: Computation of Electric Fields Using Ground Grid Performance Equations, *IEEE Trans. on Power Delivery*, Vol. 2, No. 3, pp. 709–716, July 1987.
- [11] S. Milun, T. Kilić, G. Petrović: Measurement of Magnetic Fields Generated by Different Low Frequency Electromagnetic Interference (EMI) Sources in the Zone Podi-Dugopolje, Minorm, Split, 2003. ) (in *Croatian*)
- [12] <https://www.icnirp.org/en/about-icnirp/aim-status-history/index.html>,
- [13] <https://www.icnirp.org/en/about-icnirp/aim-status-history/index.html>,
- [14] <https://www.emfs.info/limits/limits-organisations/icnirp-2010>
- [15] <https://www.emfs.info/limits/world/>
- [16] Rianne Stam, Comparison of International policies on electromagnetic fields (power frequency and radio frequency fields), National Institute for Public Health and the Environment, Ministry of Health, Welfare and Sport, The Netherlands, 2018.
- [17] Law on Protection from Non-Ionizing Radiation (Official Gazette 91/10, 114/18) (in *Croatian*)
- [18] <https://ehp.niehs.nih.gov/doi/full/10.1289/ehp.7538>
- [19] Čapeta, T., Rodin S., Fundamentals of European Union Law, 3rd Edition, Publisher: Official Gazette, 2018. (in *Croatian*)

